







# Programmable simulations of molecules and materials with reconfigurable quantum processors

Received: 22 November 2023

Accepted: 14 November 2024

Published online: 22 January 2025

 Check for updates

Nishad Maskara <sup>1,2</sup>✉, Stefan Ostermann<sup>1</sup>, James Shee <sup>3,4</sup>,  
Marcin Kalinowski <sup>1</sup>, Abigail McClain Gomez<sup>1</sup>, Rodrigo Araiza Bravo<sup>1</sup>,  
Derek S. Wang<sup>5</sup>, Anna I. Krylov<sup>6</sup>, Norman Y. Yao <sup>1</sup>, Martin Head-Gordon<sup>2,3</sup>,  
Mikhail D. Lukin <sup>1</sup>✉ & Susanne F. Yelin <sup>1</sup>✉

Simulations of quantum chemistry and quantum materials are believed to be among the most important applications of quantum information processors. However, realizing practical quantum advantage for such problems is challenging because of the prohibitive computational cost of programming typical problems into quantum hardware. Here we introduce a simulation framework for strongly correlated quantum systems represented by model spin Hamiltonians that uses reconfigurable qubit architectures to simulate real-time dynamics in a programmable way. Our approach also introduces an algorithm for extracting chemically relevant spectral properties via classical co-processing of quantum measurement results. We develop a digital–analogue simulation toolbox for efficient Hamiltonian time evolution using digital Floquet engineering and hardware-optimized multi-qubit operations to accurately realize complex spin–spin interactions. As an example, we propose an implementation based on Rydberg atom arrays. In addition, we show how detailed spectral information can be extracted from the dynamics through snapshot measurements and single-ancilla control, enabling the evaluation of excitation energies and finite-temperature susceptibilities from a single dataset. To illustrate the approach, we show how to use the method to compute key properties of a polynuclear transition-metal catalyst and two-dimensional magnetic materials.

A major thrust of quantum chemistry and material science involves the quantitative prediction of electronic structure properties of molecules and materials. Although powerful computational techniques have been developed over the past decades, especially for weakly correlated systems<sup>1–4</sup>, the development of tools for understanding and predicting the properties of materials that feature strongly correlated electrons remains a challenge<sup>5–7</sup>. Quantum computing is a promising route to efficiently capturing such quantum correlations<sup>8–10</sup>, and algorithms for

Hamiltonian simulation and energy estimation<sup>11</sup> with good asymptotic scaling have been developed. However, existing methods for simulating large-scale electronic structure problems are prohibitively expensive to run on near-term quantum hardware<sup>12</sup>, highlighting the need for more efficient approaches.

One approach to capturing the complexity of strongly correlated systems utilizes model Hamiltonians<sup>13</sup>, such as the generalized Ising, Heisenberg and Hubbard models, which describe the interactions

A full list of affiliations appears at the end of the paper. ✉ e-mail: [nmaskara@g.harvard.edu](mailto:nmaskara@g.harvard.edu); [lukin@physics.harvard.edu](mailto:lukin@physics.harvard.edu); [syelin@g.harvard.edu](mailto:syelin@g.harvard.edu)

between the active degrees of freedom at low temperatures. Like other coarse-graining or effective Hamiltonian approaches<sup>14</sup>, model parameters can be computed from an ab initio electronic structure problem using a number of classical techniques<sup>15–20</sup>. Furthermore, model Hamiltonians exhibit features such as low-degree connectivity that simplify implementation, making them particularly promising candidates for quantum simulation<sup>21–26</sup>. Although approximate, simplified model Hamiltonians have proved valuable in analysing strongly correlated problems<sup>27–29</sup> for small system sizes, where accurate but costly classical methods can be applied. However, as the system size increases, classical numerical methods struggle to reliably solve strongly correlated model systems, as the relevant low-energy states often exhibit a large degree of entanglement. In this Article, we focus on the programmable quantum simulations of spin models. These correspond to a class of Hamiltonians that describe compounds where unpaired electrons become localized at low temperatures and can therefore be represented as effective local spins with  $S \geq 1/2$ . These include many polynuclear transition metal compounds and materials containing *d*- and *f*-block elements, which play a central role in chemical catalysis and magnetism<sup>20,28,29</sup>.

Recent advances in quantum simulation<sup>30,31</sup> have enabled the study of paradigmatic model Hamiltonians with local connectivity. In particular, experiments have probed non-equilibrium quantum dynamics<sup>32–34</sup>, exotic forms of emergent magnetism<sup>35–38</sup> and long-range entangled topological matter<sup>39–41</sup> in regimes that push the limits of state-of-the-art classical simulations<sup>42</sup>. The model Hamiltonians describing realistic molecules and materials, however, often contain more complex features, including anisotropy, non-locality and higher-order interactions<sup>29</sup>, demanding a higher degree of programmability<sup>18</sup>. Although universal quantum computers can, in principle, simulate such systems, standard implementations based on local two-qubit gates require large circuit depths<sup>23</sup> to realize complex interactions and long-range connectivity. Thus, for optimal performance in devices with limited coherence, it is essential to utilize hardware-efficient capabilities to simulate such systems.

Here, we introduce a framework to simulate model spin Hamiltonians (Fig. 1) on reconfigurable quantum devices. The approach combines two elements. First, we describe a hybrid digital–analogue simulation toolbox for realizing complex spin interactions, which combines the programmability of digital simulation with the efficiency of hardware-optimized multi-qubit analogue operations. Then, we introduce an algorithm, dubbed many-body spectroscopy that leverages time dynamics and snapshot measurements to extract detailed spectral information of the model Hamiltonian in a resource-efficient way<sup>43</sup>. We describe in detail how these methods can be implemented using Rydberg atom arrays<sup>32,41</sup> and discuss its applicability to other emerging platforms that can support multi-qubit control and dynamic programmable connectivity<sup>44</sup>, such as the ion quantum charge-coupled device (QCCD) architecture<sup>45,46</sup>. Finally, we illustrate potential applications of the framework on model Hamiltonians describing a prototypical biochemical catalyst and two-dimensional (2D) materials.

## Engineering spin Hamiltonians

The general Hamiltonian we consider is

$$H = \sum_{i,\alpha} B_i^\alpha \hat{S}_i^\alpha + \sum_{ij,\alpha\beta} J_{ij}^{\alpha\beta} \hat{S}_i^\alpha \hat{S}_j^\beta + \sum_{ijk,\alpha\beta\gamma} K_{ijk}^{\alpha\beta\gamma} \hat{S}_i^\alpha \hat{S}_j^\beta \hat{S}_k^\gamma + \text{higher order}, \quad (1)$$

where  $\hat{S}_i^\alpha$ ,  $\alpha = x, y, z$  are spin- $S_i$  operators of the  $i$ th spin ( $S_i \geq 1/2$  can vary between sites), and the interaction coefficients ( $J_{ij}^{\alpha\beta}$ ,  $K_{ijk}^{\alpha\beta\gamma}$  and so on) are potentially long range ( $\hat{S}$  represents a quantum mechanical operator. We distinguish between the spin operator  $\hat{S}$  and the spin number

$S$  (no hat) throughout the paper). Hamiltonians of this form can capture the effects of many processes arising in physical compounds, including super-exchange, spin–orbit coupling, ring exchange and more<sup>29</sup>. In our approach, spin- $S$  variables are encoded into the collective spin of  $2S$  qubits, such that the  $i$ th spin in equation (1) is rewritten as

$$\hat{S}_i^\alpha = \sum_{a=1}^{2S_i} \hat{S}_{i,a}^\alpha, \quad (2)$$

where  $\hat{S}_{i,a}^\alpha$  are the spin-1/2 operators of the  $a$ th qubit in the  $i$ th spin. Valid spin- $S_i$  states live in the symmetric subspace with maximum total spin per site  $\langle (\hat{S}_i)^2 \rangle = S_i(S_i + 1)$ . While several alternate approaches to encoding spins with hardware-native qudits have been proposed recently<sup>47–50</sup>, the cluster approach introduced here uses the same controls as qubit-based computations, ensuring compatibility with existing setups<sup>51</sup>, and naturally supports simulation of models with mixed on-site spin.

The core of our protocol involves applying a  $K$ -step sequential evolution under simpler interaction Hamiltonians  $H_i = \sum_{g \in G_i} h_{i,g}$ ,  $i = 1, \dots, K$ , acting on disconnected groups  $G_i$  of a few qubits each. The combined sequence realizes an effective Floquet Hamiltonian  $H_F$  that approximates equation (1). To controllably generate effective Hamiltonians, we use the average Hamiltonian approach. In the limit of small step sizes  $\tau \ll 1/K$ , the evolution is well approximated by  $H_F^{(0)} = \frac{1}{K} \sum_{i=1}^K H_i$  to leading order, and contributions from higher-order terms are bounded<sup>52</sup>.

In general, the performance of this approach will be limited by simulation errors, characterized by the difference between  $H_F$  and the target Hamiltonian  $H$ , and gate errors, determined by the hardware overhead required to implement individual evolutions  $e^{-ih_{i,g}\tau}$ . To mitigate the leading sources of error, we next develop Hamiltonian engineering protocols that leverage multi-qubit spin operations to realize equation (1) with short periodic sequences.

## Dynamical projection with digital Floquet engineering

Our Hamiltonian engineering approach is based on the cluster encoding equation (2). The key idea is to first generate interactions in the full Hilbert space using a spin-1/2 (qubit) version  $H_i$  of equation (1) and then dynamically project back onto the encoding space. We select  $H_i$  such that projection recovers the target Hamiltonian, by mapping each  $n$ -body large spin interaction in equation (1) onto an equivalent  $n$ -body qubit interaction acting on representatives from the  $n$ -clusters (Methods and Fig. 2a). We further decompose  $H_i$  into  $D$  non-overlapping groups  $H_{i,j}$ , such that each term can be applied sequentially.

While this generates the target interactions between spin clusters, it also moves encoded states out of the symmetric subspace. Therefore, to prevent evolution under  $H_i$  from destroying the encoding, we alternately apply evolution under

$$H_p = \lambda \sum_i (1 - P(\hat{S}_i)), \quad (3)$$

composed of projectors  $P(\hat{S}_i)$  onto the symmetric spin states, by applying multi-qubit gates within spin clusters. The symmetric states are zero-energy ground states of  $H_p$ , and non-symmetric states are separated by an energy gap  $\lambda$ . Alternating  $H_i$  and  $H_p$  enables Trotter simulation of the static Hamiltonian  $H_i + H_p$ . For  $\lambda \gg J_{ij}$ , the system is effectively projected into the ground space of  $H_p$  at low energies, realizing  $H$ . However, accurate Trotter simulation in this regime, by alternating  $H_i$  and  $H_p$ , requires two separations of timescale between the step size and the target interactions  $\tau \ll \lambda^{-1} \ll J_{ij}^{-1}$ , leading to a large number of gates.

Instead, we develop an approach that enables projection of  $H_i$  onto the ground state of  $H_p$  with substantially fewer gates, using ideas

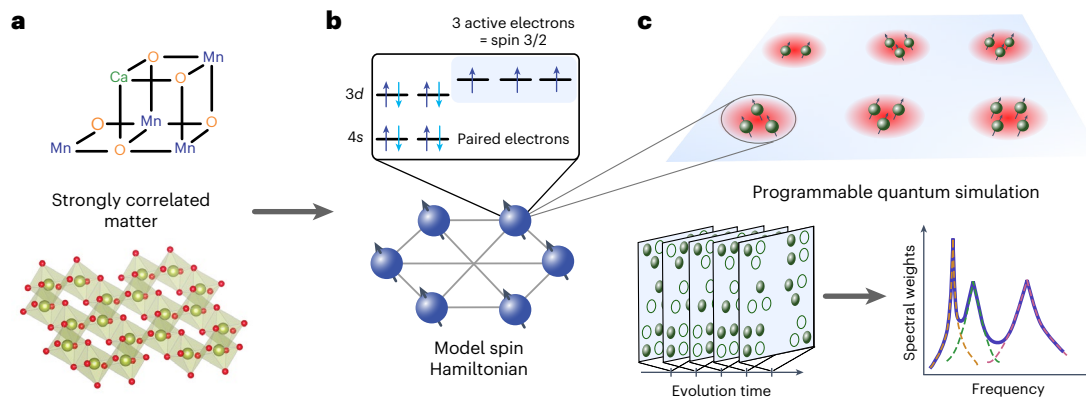


**Fig. 1 | Model Hamiltonian approach to quantum simulation of strongly correlated matter.** **a**, The procedure starts with a description of the target molecule or material structure, whose electronic structure problem is reduced using classical computational chemistry techniques to a simpler effective Hamiltonian that captures the relevant low-energy behaviours. **b**, Here, we study problems that are modelled by spin Hamiltonians with potentially non-local connectivity and generic on-site spin  $S \geq 1/2$ , where each spin is composed of localized, unpaired electrons in the original molecule. The key simplification comes from capturing charge fluctuations perturbatively, which is a good approximation in certain contexts. **c**, Programmable quantum simulation is then

used to calculate properties of the model Hamiltonian. We develop a simulation framework, based on encoding spins into clusters of qubits, that can be readily implemented on existing hardware. The toolbox enables efficient generation of complex spin interactions by leveraging dynamical reconfigurability and hardware-optimized multi-qubit gates (Figs. 2 and 3). The quantum simulator performs time evolution under the spin Hamiltonian for various simulation times  $t$ , and each qubit is projectively measured to produce an set of snapshots. Subsequent classical processing extracts properties such as the low-lying excitation spectrum and magnetic susceptibilities, all from the same dataset (Figs. 4–6).

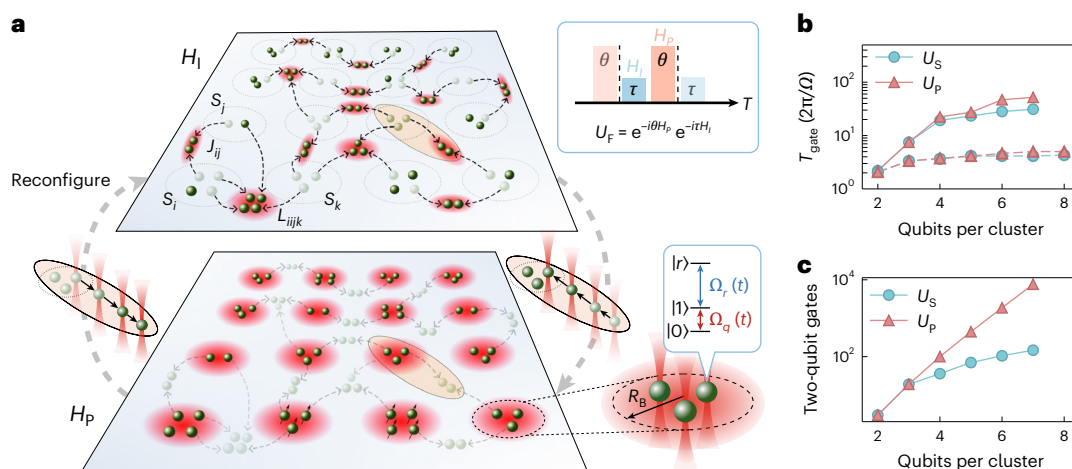


**Fig. 2 | Hardware-efficient implementation with neutral-atom tweezer arrays.** **a**, Our protocol for programmable simulation of generic spin Hamiltonian is based on applying sequences of interactions between non-overlapping few-qubit groups. Here, we illustrate an implementation of a complex spin model using the dynamical projection approach. Spin- $S$  variables are encoded in the collective spin of a cluster of  $2S$  qubits within a blockade radius  $R_B$ . Then, interactions between spins are generated by evolving pairs of qubits from each cluster under an interaction Hamiltonian  $H_I$ . Second-order interactions  $J_{ij}$  act on two qubits, while higher-order interactions act on multiple qubits, such as the fourth-order coefficient  $L_{ijkl}$  of  $S_i^\alpha S_i^\beta S_j^\gamma S_k^\delta$ . Then, interactions are dynamically projected into the symmetric encoding space within each cluster by evolving under Hamiltonian  $H_P$ . The target large spin Hamiltonian  $H$  is simulated by alternately evolving under  $H_I$  and  $H_P$ . This protocol can be realized in any reconfigurable quantum processor. Here, we present an implementation for Rydberg atom arrays, which has two long-lived qubit states  $|0\rangle$ ,  $|1\rangle$ , and an excited

Rydberg state  $|r\rangle$  with strong interactions. The interaction connectivity is dynamically changed by moving optical tweezers<sup>41</sup>, and interactions are generated using all-to-all Rydberg blockade interactions within each cluster and simultaneous global driving of the qubit  $\Omega_q(t)$  and Rydberg  $\Omega_r(t)$  transitions. **b**, Fast and efficient multi-qubit spin operations  $U_S$  and  $U_P$  are identified using optimal control to optimize pulse sequences. Gate times are measured in units of the Rydberg driving frequency  $\Omega T$ , where the two-qubit CZ gate from ref. 51 takes  $\Omega T/2\pi \approx 1.2$ . The alternating ansatz (solid lines) decomposes the target operations into symmetric diagonal gates and single-qubit rotations, which can be individually optimized (Methods). Simultaneous (dual) driving of both transitions (dotted lines) enables even faster realization of approximate  $U_S$  and  $U_P$  gates with noise-free error rates below  $10^{-3}$ . **c**, We compare against decomposition of  $U_S$  and  $U_P$  into a two-qubit gate set composed of CPhase gates and single-qubit rotations. Such a decomposition rapidly becomes very costly as the cluster size grows, in contrast to the optimized hardware-native operation.

inspired by dynamical decoupling<sup>53,54</sup>. This is achieved by using large-angle rotations  $e^{-itH_P}$ , where  $t\lambda \approx 1$ , to generate a time-dependent phase on the parts of  $H_I$  that couple encoded states to non-symmetric states. These phases cancel out on average, leaving the symmetric part which commutes with  $H_P$  (see the ‘High-spin Hamiltonian engineering with dynamical Floquet projection’ section in the Methods for details).

This approach provides important benefits in simulating complex spin models, where the number of overlapping terms in  $H$  grows rapidly with parameters such as the spin size  $S$ , number of interactions per spin  $d$  and interaction weight  $n_{\max}$ . In this regime, a Trotter decomposition of  $H$  into non-overlapping terms  $h_{i,g}$  would require a sequence of length  $K \geq d(2S)^{n_{\max}-1}$ , where  $d$  measures the number of interactions each spin

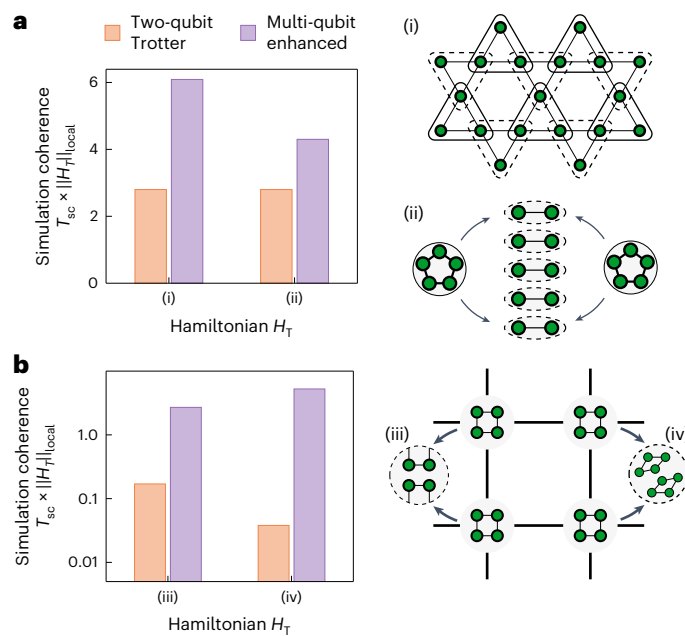


**Fig. 3 | Efficiency of Hamiltonian simulation framework.** Estimates of the quantum simulation's coherence time  $T_{sc}$ , in the target Hamiltonian's units  $\|H_T\|_{local}$  for various models. We consider Hamiltonian simulation implemented using the dual driving gates from Fig. 2b and assume a depolarizing error probability proportional to the gate time, such that  $\Omega T/2\pi = 1$  incurs an error of 0.1%, which is projected to be achievable with neutral atoms<sup>51,87,88</sup>. Analogous estimates can be performed straightforwardly for different hardware-dependent error rates using equation (32), which rescales  $T_{sc}$  but does not change the trend. In all cases, we compare against an implementation using two-qubit CPhase gates with fidelity 99.9% and perfect single-qubit rotations (see Methods for detailed descriptions of the heuristic estimation procedure). **a**, The first two two models are (i) the spin-1/2 Kagome Heisenberg model and (ii) two interacting spin-5/2's with Heisenberg and Dzyaloshinskii–Moriya (DM) terms, both of which are composed of only two-qubit interactions. In (i), a speed-up is achieved by utilizing three-qubit multi-qubit gates  $e^{-it\hat{S}_i^2}$ , which more efficiently generates Heisenberg interactions and reduces the period of the Floquet cycle from  $K = 4$  to  $K = 2$ . In (ii), improvement is achieved using dynamical projection, which reduces  $K$  from  $2S$  to 2 but at the cost of additional multi-qubit gates. **b**, Two complex spin models which include spin interactions up to (iii) bi-quadratic interactions  $J_1(\hat{S}_i \cdot \hat{S}_j) + J_2(\hat{S}_i \cdot \hat{S}_j)^2$  and (iv) bi-quartic interactions  $(\hat{S}_i \cdot \hat{S}_j)^4$ . These correspond to four-body and eight-body qubit interactions, respectively. In (iii), the dramatic speed-up originates from using dynamical projection to reduce the Floquet period, as well as the hardware efficiency of a native four-qubit gate. The individual contribution to the speed-up from both sources is also analysed in Methods. In (iv), the speed-up arises fully from the hardware efficiency of native eight-qubit operations.

$S_i$  is involved in. Instead, the projection approach produces decompositions of  $H$  into sequences of length  $K = (n_{max} + 1)\lceil \frac{d}{2S} \rceil$ , leading to performance improvements of several orders of magnitude for models with large spins and higher-order interactions.

Similar tools can also be used to realize a large class of spin circuits, by generating different evolutions  $H_{F,i}$  during each cycle. This effectively implements discrete time-dependent evolution

$$U_{circ} = \prod_{i=1}^T e^{-it_i H_{F,i}}. \quad (4)$$

Variational optimization can be further used to engineer higher-order terms in  $H_F$ , enabling the generation of more complex spin gates at no additional cost (Extended Data Fig. 1). Although the classical variational optimization procedure is limited to small circuits, Hamiltonian learning protocols could be used to perform larger-scale

optimization on a quantum device directly<sup>55</sup>. Such circuits can be used for operations besides Hamiltonian simulation, including state preparation<sup>21</sup>.

## Hardware-efficient implementation

The digital Hamiltonian engineering sequence can, in principle, be realized on any universal quantum processor, but it is especially well suited for reconfigurable processors with native multi-qubit interactions<sup>41,44,46,56</sup>. Neutral atom arrays are a particularly promising candidate for realizing these techniques, for which we develop a detailed implementation proposal. In this platform, two long-lived atomic states encode the qubit degree of freedom  $\{|0\rangle, |1\rangle\}$ , which can be individually manipulated with fidelity above 99.99% (ref. 57). Strong interactions between qubits are realized by coupling to a Rydberg state  $|r\rangle$  (ref. 58), which enables parallel multi-qubit operations<sup>57</sup>, with state-of-the-art two-qubit gate fidelities exceeding 99.5% (ref. 51). Further, qubits can be transported with high fidelity by moving optical tweezers<sup>41</sup>, to realize arbitrary groupings  $G_r$ . By placing atoms sufficiently close together, atoms within a group can undergo strong all-to-all interactions, while interactions between groups can be made negligible by placing them far apart.

The key ingredient required for efficiently implementing  $H_i$  and  $H_p$  are hardware-efficient multi-qubit spin operations. We show how these can be realized by using pulse engineering to transform the native Rydberg-blockade interaction into the desired form. We illustrate this on two families of representative spin operations

$$U_S(\theta) = e^{-i\theta(\hat{S}_i^2/2S)}, \quad U_P(\theta) = e^{-i\theta P[\hat{S}_i^2]}, \quad (5)$$

where  $\hat{S}_i^2$  is the total-spin operator for a cluster of  $2S_i$  atoms, and  $P[\hat{S}_i^2]$  are the projectors appearing in equation (3).

One approach to engineering these operations is based on an ansatz that naturally extends ref. 51, where  $U_S$  and  $U_P$  are found by optimizing an alternating sequence of diagonal phase gates and single-qubit rotations. As in prior works<sup>51,59</sup>, the pulse profiles generating symmetric diagonal operations can be obtained with numerical optimization via gradient ascent pulse engineering (GRAPE)<sup>60</sup>. For this alternating ansatz, we find a roughly linear scaling of total gate time  $T_{gate}$  with size of the cluster (Fig. 2b). Similar gates can also be implemented in ion-trap architectures, where coupling to collective motional modes can be used to implement diagonal phase gates<sup>61,62</sup>.

However, Rydberg atom arrays offer additional control, which allows us to go beyond the alternating ansatz. Specifically, we consider simultaneously driving the qubit transition  $\Omega_q(t)$  in addition to the usual Rydberg transition  $\Omega_r(t)$ . We find that this dual driving enables substantially faster realizations of  $U_S$  and  $U_P$ . After optimizing with GRAPE to identify approximate gates with noise-free simulated fidelities above 99.9% (that is, assuming no experimental error), we find total gate times below  $\Omega T_{gate}/2\pi = 6.0$  up to cluster sizes  $n = 8$  and nearly constant scaling with  $n$  (Fig. 2b and Methods). The fact that the evolution is so short implies that these gates generate complex interactions in a very hardware-efficient way, making them ideal for accelerating spin-Hamiltonian simulations. Finally, we develop optimized decompositions of target spin operations into two-qubit gates and find they are still orders of magnitude more costly than the hardware-efficient implementation (Fig. 2c).

In Fig. 3, we illustrate the performance of this method on four representative examples that lie within the family of Hamiltonians (equation (1)). To quantify the performance of the simulation, we present heuristic estimates of the accessible coherent simulation time, measured in units of the target Hamiltonian's local energy scale. We leverage access to multi-qubit spin operations of the form  $e^{-i\sum_n \theta_n \hat{S}_i^n}$  and estimate gate errors (arising from experimental imperfections) based on the physical evolution time necessary to realize the target

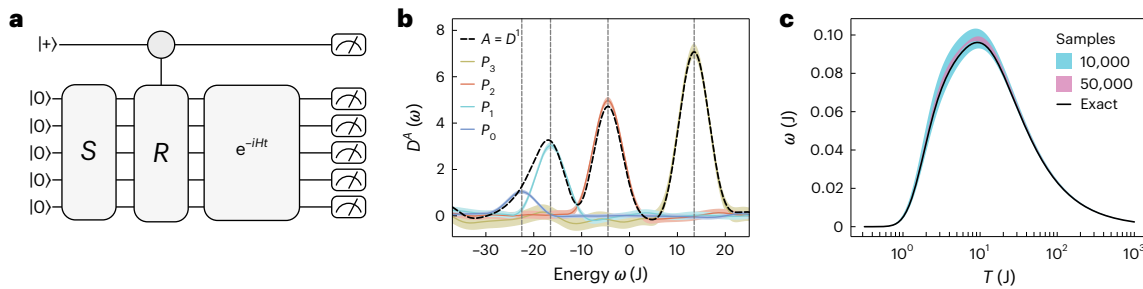


**Fig. 4 | Many-body spectroscopy of model Hamiltonians.** **a**, A schematic quantum circuit diagram for the algorithm. The first step is to apply a state-preparation circuit  $S$  to prepare a reference state  $|S\rangle = S|0\rangle$ , followed by an ancilla-controlled perturbation  $R$  preparing a superposition of  $|S\rangle$  and the probe state  $|R\rangle = R|S\rangle$ . This superposition is time-evolved by the target Hamiltonian, and then each qubit is projectively measured to produce a snapshot. By repeating the procedure for various evolution times  $t$ , different perturbations  $R$  and potentially different measurement bases, this setup provides access to detailed information about the spectrum of  $H$ . **b**, Consider a spin Hamiltonian  $H_2$  with two anti-ferromagnetically coupled spin-3/2 particles. We simulate 20,000 snapshot measurements and classical processing to calculate the density of states  $D^1(\omega)$  (black line) and total-spin resolved versions  $D^S(\omega)$  (coloured lines). The vertical dashed lines correspond to exact energies, and the coloured regions represent 95% confidence intervals. The peaks are broadened due to finite (coherent)

simulation time  $JT_{\text{sim}} = 0.26$ , which sets the spectral resolution. Hardware-efficient simulation schemes, which extend the simulation time (for example, Fig. 3), are favourable because they improve spectral resolution. Many-body spectroscopy further improves the effective spectral resolution, by leveraging multiple observables to distinguish overlapping peaks. Here, we see that spin resolution sparsifies the signal, enabling accurate peak detection and energy estimation, while the bare spectrum  $D^1(\omega)$  is too broad to resolve all states. **c**, The magnetic susceptibility  $\chi$ , can also be computed from snapshot measurements using  $S^z$ -resolved density of states (here,  $JT_{\text{sim}} = 1.04$ ). For these calculations, it is important to prevent exponential amplification of shot noise. We therefore use a simple empirical truncation procedure that introduces a small amount of bias (Methods) but enables rapid convergence with number of snapshots to the ideal value (black line).

operation. The step size  $\tau$  is chosen to maximize coherent simulation time, balancing simulation and gate errors (Methods). In the representative examples, we find the combination of dynamical projection and optimized multi-qubit gates outperforms a similarly constructed implementation based on Trotterized interactions and two-qubit gate decomposition. Our approach substantially extends the available simulation time (up to two orders of magnitude) and enables much more efficient generation of complex spin Hamiltonians.

### Spectral information from dynamics

Having described a toolbox for implementing a large class of spin circuits, enabling time evolution and state preparation, we next present a general-purpose algorithm for calculating chemically relevant information. The approach, dubbed many-body spectroscopy, leverages dynamical snapshot measurements and classical co-processing<sup>43</sup> to compute a wide variety of spectral quantities including low-lying states and finite-temperature properties. The procedure, combining insights from statistical phase estimation<sup>63–66</sup> and shadow tomography<sup>67</sup>, is noise resilient and sample efficient, making it especially promising for near-term experiments.

Specifically, the quantity we extract is an operator-resolved density of states

$$D^A(\omega) = \sum_n \langle n|A|n\rangle \delta(\omega - \epsilon_n), \quad (6)$$

where  $\epsilon_n$  and  $|n\rangle$  are the energies and eigenstates of the evolution Hamiltonian  $H$ , and  $A$  denotes an arbitrary operator. Spectral functions like equation (6) can be used to access detailed information about the properties of  $H$ : the location of peaks provides information about energies<sup>63,65,66</sup>, and properties of eigenstates can be computed by choosing  $A$  appropriately<sup>64</sup>. For example, we can compute total-spin of an eigenstate using  $A = (\sum_i \hat{S}_i)^2$  or the local spin polarization with  $A = \hat{S}_i$ .

The output of the quantum computation are projective measurements (snapshots), produced by the circuit depicted in Fig. 4a. First, we initialize a system of  $N$  qubits and apply a state preparation procedure to prepare a reference state  $|S\rangle = S|0^N\rangle$ . Next, we use a single-ancilla qubit in the  $|+\rangle$  state to apply a controlled perturbation, preparing an entangled superposition of  $|0\rangle|S\rangle$  and a probe state  $|1\rangle|R\rangle$

where  $|R\rangle = R|S\rangle$ . The system is then evolved under  $H$  for time  $t$  (see also equation (34)). Finally each qubit is projectively measured, producing a sequence of  $N + 1$  bits—a snapshot. By measuring the ancilla in the  $X$  or  $Y$  basis, this circuit effectively performs an interferometry experiment between the reference and probe states. The resulting snapshot measurements enable parallel estimation of two-time correlation functions of the form  $C_{O,R}(t) = \langle S|e^{iHt}Oe^{-iHt}R|S\rangle$  for all  $2^N$  operators  $O$  that are diagonal in the measurement basis. Crucially,  $D^A(\omega)$  can be determined from the same set of snapshots for various  $A$  and  $\omega$ , by changing the classical processing.

To estimate the spectral function  $D^A(\omega)$ , we use a hybrid quantum-classical computation based on the expression

$$D^A(\omega) = \underbrace{\mathbb{E}_{R \sim \mathcal{R}}}_{\text{circuit average}} \int dt e^{i\omega t} \underbrace{\sum_S \langle S|R^\dagger A O_S e^{-iHt}|S\rangle}_{\text{classical processing}} \times \underbrace{\langle S|e^{iHt}O_S e^{-iHt}R|S\rangle}_{\text{quantum evolution (Fig. 4)}}. \quad (7)$$

For this to be formally equivalent to equation (6), the distribution over perturbations  $\mathcal{R}$  and ensemble of observables  $\{O_S\}$  must couple uniformly to all eigenstates, to ensure unbiased estimation (Methods). For example, given a polarized reference state  $|0\rangle^{\otimes N}$ ,  $X$ -basis measurements are sufficient.

To realize the distributional average and time integral, the quantum circuit has to be executed (Fig. 4a) for randomly sampled perturbations  $R$  and evolution times  $t$ . To efficiently evaluate the classical part of equation (7), we require efficient classical representations of  $|R\rangle$  and  $e^{-iHt}|S\rangle$ . A good choice is to select  $|S\rangle$  to be a known eigenstate of  $H$ , such that the time evolution is trivial, and preferentially sample  $|R\rangle$  to maximize the overlap with relevant target states. By contrast, the quantum part of equation (7) includes the time evolution of  $|R\rangle$ , which has overlap with unknown eigenstates, and often includes large amounts of entanglement. Therefore, this is estimated from snapshot measurements produced by quantum simulation (Methods).

As an example, consider two interacting spin-3/2 particles, described by  $H_2 = J\mathbf{S}_1 \cdot \mathbf{S}_2$ . We prepare a polarized reference eigenstate  $|S\rangle = |0\rangle^{\otimes 6}$ , and sample perturbations  $R$  from an ensemble of random

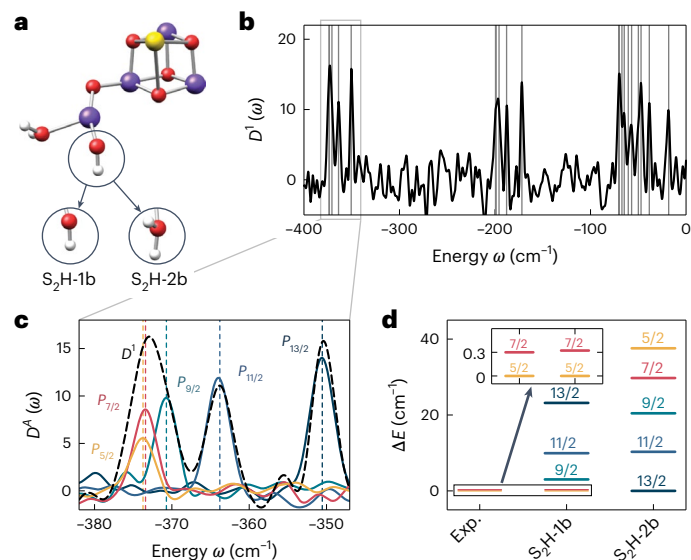


**Fig. 5 | Application to the OEC.** Our programmable quantum simulation framework can be used to compute detailed model spin Hamiltonian properties. **a**, Here, we illustrate the procedure on the OEC, an organometallic catalyst with strong spin correlations. In particular, we simulate model spin Hamiltonians for two structures  $S_2H-1b$  and  $S_2H-2b$ , which have three spin-3/2 and one spin-2 Mn (purple) active sites (reproduced from ref. 28 with permission from the Royal Society of Chemistry). Model Heisenberg coefficients for both hypothetical structures have been computed from broken-symmetry DFT<sup>28</sup>. **b**, A density of states  $D^1(\omega)$  calculation is simulated for the  $S_2H-1b$  model spin Hamiltonian. Here, we use a polarized reference state  $|S\rangle = |0\rangle^{\otimes 13}$  a probe states  $|R\rangle$  generated by random single-site rotations and an evolution time  $t$ . We select 50,000 circuits with independently chosen  $|R\rangle$ ,  $t$  pairs and draw ten snapshots from each circuit. **c**, Focusing on the lowest-lying states, we see three distinct peaks in  $D^1(\omega)$ . However, by evaluating spin-resolved quantities  $D^{P_s}(\omega)$  on the same set of measurements, we identify three additional peaks, whose energies and total-spin match exact diagonalization results (vertical dotted lines). **d**, This information is known as the spin ladder and can be computed using many-body spectroscopy for both the 1b and 2b states. Importantly, the spin ladder can also be measured experimentally (Exp.) and, therefore, can be used to help determine which structure appears in nature. In this example, experimental measurements indicate a spin-5/2 ground state and spin-7/2 first excited state. However, the ordering of low-energy states is flipped in the 2b configuration, indicating that the  $S_2H-1b$  hypothesis is more likely<sup>28</sup>. We note that quantities beyond total spin can also be readily evaluated in low-lying eigenstates by inserting different operators  $A$  (Methods).

single-spin rotations. This corresponds to a trivial state-preparation circuit and a simple controlled-perturbation composed of two-qubit gates in Fig. 4. Next, we measure the system in the  $X$  basis, which provides access to the full spectrum for this choice of  $|S\rangle$  (Methods). Finally, during classical processing, the bare density of states is obtained by choosing  $A = \mathbb{1}$  and evaluating equation (7). The result contains peaks at frequencies  $\omega$  associated with eigenstates of  $H_2$  (Fig. 4b). Further, we can isolate individual contributions of total spin sectors by instead choosing  $A = P_s$ , the projectors onto  $S = 0, 1, 2$  and 3. This not only allows us to identify the total spin of the eigenstates but also increases the effective spectral resolution in the presence of noise as it sparsifies the signal. Finite-temperature response functions<sup>68</sup>, such as the  $z$  component of the zero-field magnetic susceptibility  $\chi(T) = \frac{1}{Z} \text{Tr}[\frac{1}{T}(S_z)^2 e^{-H/T}]$ , can also be computed from the same dataset, by integrating the  $S_z$ -projected density-of-states  $D^{S_z}(\omega)$  (Methods). To illustrate this, the magnetic susceptibility is extracted from the same dataset and shown in Fig. 4c. The algorithm is especially promising for near-term devices, having favourable resource requirements quantified by the number of snapshots (sample complexity) and maximum evolution time

(coherence) required for accurate spectral computation (see Methods for further discussion).

## Application to transition metal clusters and magnetic solids

As an illustration of a relevant computation in chemical catalysis, we consider the  $Mn_4O_5Ca$  core of the oxygen-evolving complex (OEC), a transition metal catalyst central to photosynthesis that is still not fully understood<sup>69,70</sup>. Classical chemistry calculations have been used to fit model Heisenberg Hamiltonians, containing three spin-3/2 sites and one spin-2 site<sup>27,28</sup> (Fig. 5a). While this spin representation cannot directly capture chemical reactions, it can capture the ground and low-lying spin states, that is, the spin ladder, which are important in catalysis because reaction pathways depend critically on the spin multiplicity<sup>71</sup>. We simulate our framework applied to the  $S_2H-1b$  structural model from ref. 28, by first computing the bare density of states  $D^1(A)$  (Fig. 5b). Then, we identify a low-lying cluster of eigenstates and compute spin-projected densities  $D^{P_s}(A)$  to resolve the spin ladder (Fig. 5c). The spin ladder can also be measured experimentally, providing a way to evaluate candidate models of reaction intermediates. To highlight this, we simulate the Heisenberg model for an alternate pathway ( $S_2H-2b$ )<sup>28</sup> and observe the modification reverses the ordering of the spin ladder, indicating that  $S_2H-1b$  is more consistent with measurements (Fig. 5d).

The framework can also be applied to study low-energy properties of extended systems, including strongly correlated materials. We

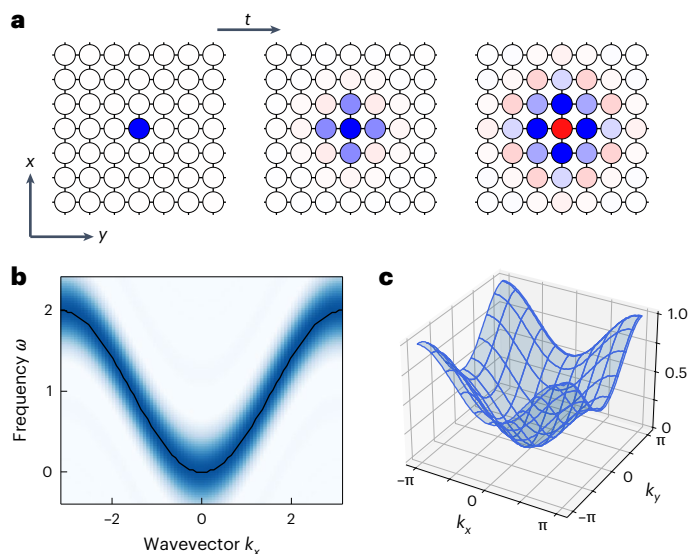


**Fig. 6 | Application to 2D magnetic materials.** **a**, Properties of extended materials can also be investigated using our quantum simulation framework. As an example, we study the square-lattice ferromagnetic ( $J > 0$ ) Heisenberg model  $H_{2D} = -J \sum_{\langle ij \rangle} \hat{s}_i \cdot \hat{s}_j$ . By preparing the polarized ground state  $|S\rangle = |0\rangle^{\otimes N}$ , applying a single-site perturbation  $R = X_0$  on the central site and measuring the system in the  $X$  basis after time evolution, we can estimate the single-particle Green's function  $G(\mathbf{r}, t) = \langle S|X_r(t)X_0|S\rangle$ . Therefore we select  $O = X_r$  for various positions  $\mathbf{r}$  as the observables in equation (7), all of which are diagonal in the measurement basis. We visualize the real part of  $G(\mathbf{r}, t)$ , where the plotted intensity and colour denotes the magnitude and sign, respectively, at  $t = 0, 0.5$  and  $1.0$ . **b**, The structure of excited states is extracted by classical processing of these measurements. Even though the spectrum is continuous, additional structure can be identified by computing the momentum-resolved density of states  $D^{P_{\mathbf{k}}}(\omega)$ , where  $P_{\mathbf{k}}$  is a projector onto plane-wave states (Methods). Restricting to  $k_y = 0$  and evolving to maximum time  $JT_{\max} = 8.0$ , we see  $D^{P_{\mathbf{k}}}(\omega)$  forms a band-like structure, from which a peak  $\omega$  can be estimated for each  $\mathbf{k}$  (black line). **c**, This peak extraction allows us to directly estimate the single-particle dispersion  $\omega(\mathbf{k})$  across the 2D Brillouin zone.

illustrate this on the ferromagnetic, square lattice Heisenberg model (Fig. 6). For such large systems, we envision utilizing an approximate ground-state preparation method for  $|S\rangle$ , so that low-energy properties can be accessed in a noise resilient manner via local controlled perturbations  $R$ . Then, local Green's functions—two-point operators at different positions and times—can be measured to access properties of low-lying quasi-particle excitations, such as the dispersion relation of single-particle excitations (see 'Two-dimensional Heisenberg calculations' section in Methods for details).

## Outlook

These considerations indicate that reconfigurable quantum processors enable a powerful, hardware-efficient framework for quantum simulation of problems from chemistry and materials science, illustrating potential directions for the search for useful quantum advantage. Specifically, in addition to the OEC, other organometallic catalysts could be studied with this approach, including iron–sulfur clusters<sup>23,72</sup>, for which bi-quadratic terms appear in the model Hamiltonian to capture higher-order perturbative charge fluctuation effects<sup>73</sup>. Another promising direction involves quantum simulation of low-energy properties of 2D and three-dimensional frustrated spin systems, including model Hamiltonians for Kitaev materials<sup>74–76</sup> and molecular magnets<sup>77,78</sup>. The ability to realize non-local interactions further opens the door to simulation of spin Hamiltonians defined on non-Euclidean interaction geometries<sup>79,80</sup>.

The efficiency of the Hamiltonian engineering approach originates from co-designing Floquet engineering and hardware-specific multi-qubit gates. Extending this approach to larger classes of strongly correlated model Hamiltonians is an outstanding and exciting frontier. In particular, it would be especially interesting to further develop the toolbox to incorporate charge transport and electron–phonon interactions. This could enable simulation of more complex model Hamiltonians, such as the  $t$ - $J$ , Hubbard and Hubbard–Holstein models, and expand the class of accessible chemistry problems<sup>9,81</sup>. Application to other settings, including lattice gauge theories<sup>50</sup> and quantum optimization problems<sup>82</sup>, is also of interest. Incorporation of error mitigation and correction into the Hamiltonian simulation should be considered; specifically, the present method can potentially be generalized to control logical, encoded degrees of freedom in a hardware-efficient way<sup>83</sup>.

Finally, characterization and development of the model Hamiltonian approach itself is an interesting and challenging problem. Key challenges include development of efficient schemes to compute parameters for higher-order interactions<sup>73</sup>, estimation of corrections arising from coupling to states outside the model space<sup>84</sup> and validation of the model Hamiltonian approximation<sup>19</sup>. Feedback between the classical and quantum parts of the computation is an important part of these developments<sup>25,85,86</sup>. For these reasons, the large-scale simulation of model Hamiltonians on quantum processors will be invaluable for testing approximations by comparing simulation outputs with experimental measurements. Hence, the approach proposed in this work facilitates exciting directions in computational chemistry and quantum simulation, aiming towards constructing a novel ab initio simulation pipeline that utilizes hybrid quantum-classical resources.

## Online content

Any methods, additional references, Nature Portfolio reporting summaries, source data, extended data, supplementary information, acknowledgements, peer review information; details of author contributions and competing interests; and statements of data and code availability are available at <https://doi.org/10.1038/s41567-024-02738-z>.

## References

1. Szabo, A. & Ostlund, N. S. *Modern Quantum Chemistry: Introduction to Advanced Electronic Structure Theory* (Courier Corporation, 2012).
2. Bartlett, R. J. & Musiał, M. Coupled-cluster theory in quantum chemistry. *Rev. Mod. Phys.* **79**, 291–352 (2007).
3. Mardirossian, N. & Head-Gordon, M. Thirty years of density functional theory in computational chemistry: an overview and extensive assessment of 200 density functionals. *Mol. Phys.* **115**, 2315–2372 (2017).
4. Burke, K. Perspective on density functional theory. *J. Chem. Phys.* **136**, 150901 (2012).
5. Aoto, Y. A., de Lima Batista, A. P., Kohn, A. & de Oliveira-Filho, A. G. S. How to arrive at accurate benchmark values for transition metal compounds: computation or experiment? *J. Chem. Theory Comput.* **13**, 5291–5316 (2017).
6. Hait, D., Tubman, N. M., Levine, D. S., Whaley, K. B. & Head-Gordon, M. What levels of coupled cluster theory are appropriate for transition metal systems? a study using near-exact quantum chemical values for 3d transition metal binary compounds. *J. Chem. Theory Comput.* **15**, 5370–5385 (2019).
7. Ahn, C. et al. Designing and controlling the properties of transition metal oxide quantum materials. *Nat. Mater.* **20**, 1462–1468 (2021).
8. Alexeev, Y. et al. Quantum computer systems for scientific discovery. *PRX Quantum* **2**, 017001 (2021).
9. Bauer, B., Bravyi, S., Motta, M. & Chan, G. K.-L. Quantum algorithms for quantum chemistry and quantum materials science. *Chem. Rev.* **120**, 12685–12717 (2020).
10. McArdle, S., Endo, S., Aspuru-Guzik, A., Benjamin, S. C. & Yuan, X. Quantum computational chemistry. *Rev. Mod. Phys.* **92**, 015003 (2020).
11. Lin, L. Lecture notes on quantum algorithms for scientific computation. Preprint at <https://arxiv.org/abs/2201.08309> (2022).
12. Beverland, M. E. et al. Assessing requirements to scale to practical quantum advantage. Preprint at <https://arxiv.org/abs/2211.07629> (2022).
13. Auerbach, A. *Interacting Electrons and Quantum Magnetism* (Springer, 1998).
14. Bauman, N. P., Low, G. H. & Kowalski, K. Quantum simulations of excited states with active-space downfolded Hamiltonians. *J. Chem. Phys.* **151**, 234114 (2019).
15. Bolvin, H. From ab initio calculations to model Hamiltonians: the effective Hamiltonian technique as an efficient tool to describe mixed-valence molecules. *J. Phys. Chem. A* **107**, 5071–5078 (2003).
16. Mayhall, N. J. & Head-Gordon, M. Computational quantum chemistry for single Heisenberg spin couplings made simple: just one spin flip required. *J. Chem. Phys.* **141**, 134111 (2014).
17. Mayhall, N. J. & Head-Gordon, M. Computational quantum chemistry for multiple-site Heisenberg spin couplings made simple: still only one spin-flip required. *J. Phys. Chem. Lett.* **6**, 1982–1988 (2015).
18. Pokhilko, P. & Krylov, A. I. Effective Hamiltonians derived from equation-of-motion coupled-cluster wave functions: theory and application to the Hubbard and Heisenberg Hamiltonians. *J. Chem. Phys.* **152**, 094108 (2020).
19. Kotaru, S., Kähler, S., Alessio, M. & Krylov, A. I. Magnetic exchange interactions in binuclear and tetranuclear iron(III) complexes described by spin-flip DFT and Heisenberg effective Hamiltonians. *J. Comput. Chem.* **44**, 367–380 (2023).
20. Chen, D.-T. et al. Using hyperoptimized tensor networks and first-principles electronic structure to simulate the experimental properties of the giant {Mn84} Torus. *J. Phys. Chem. Lett.* **13**, 2365–2370 (2022).
21. Kandala, A. et al. Hardware-efficient variational quantum eigensolver for small molecules and quantum magnets. *Nature* **549**, 242–246 (2017).

22. Chiesa, A. et al. Quantum hardware simulating four-dimensional inelastic neutron scattering. *Nat. Phys.* **15**, 455–459 (2019).
23. Tazhigulov, R. N. et al. Simulating models of challenging correlated molecules and materials on the sycamore quantum processor. *PRX Quantum* **3**, 040318 (2022).
24. Wecker, D. et al. Solving strongly correlated electron models on a quantum computer. *Phys. Rev. A* **92**, 062318 (2015).
25. Bauer, B., Wecker, D., Millis, A. J., Hastings, M. B. & Troyer, M. Hybrid quantum-classical approach to correlated materials. *Phys. Rev. X* **6**, 031045 (2016).
26. Ma, H., Govoni, M. & Galli, G. Quantum simulations of materials on near-term quantum computers. *npj Comput. Mater.* **6**, 85 (2020).
27. Krewald, V., Neese, F. & Pantazis, D. A. On the magnetic and spectroscopic properties of high-valent  $\text{Mn}_3\text{CaO}_4$  cubanes as structural units of natural and artificial water-oxidizing catalysts. *J. Am. Chem. Soc.* **135**, 5726–5739 (2013).
28. Krewald, V. et al. Metal oxidation states in biological water splitting. *Chem. Sci.* **6**, 1676–1695 (2015).
29. Malrieu, J. P., Caballol, R., Calzado, C. J., de Graaf, C. & Guihéry, N. Magnetic interactions in molecules and highly correlated materials: physical content, analytical derivation, and rigorous extraction of magnetic Hamiltonians. *Chem. Rev.* **114**, 429–492 (2014).
30. Monroe, C. et al. Programmable quantum simulations of spin systems with trapped ions. *Rev. Mod. Phys.* **93**, 025001 (2021).
31. Daley, A. J. et al. Practical quantum advantage in quantum simulation. *Nature* **607**, 667–676 (2022).
32. Bernien, H. et al. Probing many-body dynamics on a 51-atom quantum simulator. *Nature* **551**, 579–584 (2017).
33. Keesling, A. et al. Quantum Kibble–Zurek mechanism and critical dynamics on a programmable Rydberg simulator. *Nature* **568**, 207–211 (2019).
34. Bluvstein, D. et al. Controlling quantum many-body dynamics in driven Rydberg atom arrays. *Science* **371**, 1355–1359 (2021).
35. Labuhn, H. et al. Tunable two-dimensional arrays of single Rydberg atoms for realizing quantum Ising models. *Nature* **534**, 667–670 (2016).
36. Ebadi, S. et al. Quantum phases of matter on a 256-atom programmable quantum simulator. *Nature* **595**, 227–232 (2021).
37. Scholl, P. et al. Quantum simulation of 2D antiferromagnets with hundreds of Rydberg atoms. *Nature* **595**, 233–238 (2021).
38. Chen, C. et al. Continuous symmetry breaking in a two-dimensional Rydberg array. *Nature* **616**, 691–695 (2023).
39. Semeghini, G. et al. Probing topological spin liquids on a programmable quantum simulator. *Science* **374**, 1242–1247 (2021).
40. Satzinger, K. J. et al. Realizing topologically ordered states on a quantum processor. *Science* **374**, 1237–1241 (2021).
41. Bluvstein, D. et al. A quantum processor based on coherent transport of entangled atom arrays. *Nature* **604**, 451–456 (2022).
42. Kim, Y. et al. Evidence for the utility of quantum computing before fault tolerance. *Nature* **618**, 500–505 (2023).
43. Chan, H. H. S., Meister, R., Goh, M. L. & Koczor, B. Algorithmic shadow spectroscopy. Preprint at <https://arxiv.org/abs/2212.11036> (2023).
44. Katz, O., Feng, L., Risinger, A., Monroe, C. & Cetina, M. Demonstration of three- and four-body interactions between trapped-ion spins. *Nat. Phys.* **19**, 1452–1458 (2023).
45. Häffner, H., Roos, C. F. & Blatt, R. Quantum computing with trapped ions. *Phys. Rep.* **469**, 155–203 (2008).
46. Moses, S. A. et al. A race track trapped-ion quantum processor. *Phys. Rev. X* **13**, 041052 (2023).
47. Kruckenhauser, A., van Bijnen, R., Zache, T. V., Di Liberto, M. & Zoller, P. High-dimensional  $\text{SO}(4)$ -symmetric Rydberg manifolds for quantum simulation. *Quantum Sci. Technol.* **8**, 015020 (2022).
48. Chi, Y. et al. A programmable qudit-based quantum processor. *Nat. Commun.* **13**, 1166 (2022).
49. Hrmo, P. et al. Native qudit entanglement in a trapped ion quantum processor. *Nat. Commun.* **14**, 2242 (2023).
50. González-Cuadra, D., Zache, T. V., Carrasco, J., Kraus, B. & Zoller, P. Hardware efficient quantum simulation of non-Abelian gauge theories with qudits on Rydberg platforms. *Phys. Rev. Lett.* **129**, 160501 (2022).
51. Evered, S. J. et al. High-fidelity parallel entangling gates on a neutral-atom quantum computer. *Nature* **622**, 268–272 (2023).
52. Abanin, D. A., De Roeck, W., Ho, W. W. & Huveneers, F. Effective Hamiltonians, prethermalization, and slow energy absorption in periodically driven many-body systems. *Phys. Rev. B* **95**, 014112 (2017).
53. Choi, J. et al. Robust dynamic Hamiltonian engineering of many-body spin systems. *Phys. Rev. X* **10**, 031002 (2020).
54. Else, D. V., Bauer, B. & Nayak, C. Prethermal phases of matter protected by time-translation symmetry. *Phys. Rev. X* **7**, 011026 (2017).
55. Carrasco, J., Elben, A., Kokail, C., Kraus, B. & Zoller, P. Theoretical and experimental perspectives of quantum verification. *PRX Quantum* **2**, 010102 (2021).
56. Lis, J. W. et al. Mid-circuit operations using the omg-architecture in neutral atom arrays. *Phys. Rev. X* **13**, 041035 (2023).
57. Levine, H. et al. Parallel implementation of high-fidelity multi-qubit gates with neutral atoms. *Phys. Rev. Lett.* **123**, 170503 (2019).
58. Jaksch, D. et al. Fast quantum gates for neutral atoms. *Phys. Rev. Lett.* **85**, 2208–2211 (2000).
59. Jandura, S. & Pupillo, G. Time-optimal two- and three-qubit gates for Rydberg atoms. *Quantum* **6**, 712 (2022).
60. Khaneja, N., Reiss, T., Kehlet, C., Schulte-Herbrüggen, T. & Glaser, S. J. Optimal control of coupled spin dynamics: design of NMR pulse sequences by gradient ascent algorithms. *J. Magn. Reson.* **172**, 296–305 (2005).
61. Sørensen, A. & Mølmer, K. Quantum computation with ions in thermal motion. *Phys. Rev. Lett.* **82**, 1971–1974 (1999).
62. Katz, O., Cetina, M. & Monroe, C. N-body interactions between trapped ion qubits via spin-dependent squeezing. *Phys. Rev. Lett.* **129**, 063603 (2022).
63. Lin, L. & Tong, Y. Heisenberg-limited ground state energy estimation for early fault-tolerant quantum computers. *PRX Quantum* **3**, 010318 (2022).
64. Lu, S., Bañuls, M., MariCarmen & Cirac, J. I. Algorithms for quantum simulation at finite energies. *PRX Quantum* **2**, 020321 (2021).
65. Somma, R. D. Quantum eigenvalue estimation via time series analysis. *New J. Phys.* **21**, 123025 (2019).
66. O’Brien, T. E., Tarasinski, B. & Terhal, B. M. Quantum phase estimation of multiple eigenvalues for small-scale (noisy) experiments. *New J. Phys.* **21**, 023022 (2019).
67. Huang, Hsin-Yuan, Kueng, R. & Preskill, J. Predicting many properties of a quantum system from very few measurements. *Nat. Phys.* **16**, 1050–1057 (2020).
68. Alessio, M. & Krylov, A. I. Equation-of-motion coupled-cluster protocol for calculating magnetic properties: theory and applications to single-molecule magnets. *J. Chem. Theory Comput.* **17**, 4225–4241 (2021).
69. Askerka, M., Brudvig, G. W. & Batista, V. S. The  $\text{O}_2$ -evolving complex of photosystem II: recent insights from quantum mechanics/molecular mechanics (QM/MM), extended X-ray absorption fine structure (EXAFS), and femtosecond X-ray crystallography data. *Acc. Chem. Res.* **50**, 41–48 (2017).
70. Paul, S., Neese, F. & Pantazis, D. A. Structural models of the biological oxygen-evolving complex: achievements, insights, and challenges for biomimicry. *Green Chem.* **19**, 2309–2325 (2017).



71. Shaik, S., Hirao, H. & Kumar, D. Reactivity of high-valent iron–oxo species in enzymes and synthetic reagents: a tale of many states. *Acc. Chem. Res.* **40**, 532–542 (2007).
72. Li, Z., Guo, S., Sun, Q. & Chan, G. K.-L. Electronic landscape of the P-cluster of nitrogenase as revealed through many-electron quantum wavefunction simulations. *Nat. Chem.* **11**, 1026–1033 (2019).
73. Sharma, S., Sivalingam, K., Neese, F. & Chan, G. K.-L. Low-energy spectrum of iron-sulfur clusters directly from many-particle quantum mechanics. *Nat. Chem.* **6**, 927–933 (2014).
74. Jin, Hui-Ke, Natori, W. M. H., Pollmann, F. & Knolle, J. Unveiling the  $S=3/2$  Kitaev honeycomb spin liquids. *Nat. Commun.* **13**, 3813 (2022).
75. Xu, C. et al. Possible Kitaev quantum spin liquid state in 2D materials with  $S = 3 / 2$ . *Phys. Rev. Lett.* **124**, 087205 (2020).
76. Takagi, H., Takayama, T., Jackeli, G., Khaliullin, G. & Nagler, S. E. Concept and realization of Kitaev quantum spin liquids. *Nat. Rev. Phys.* **1**, 264–280 (2019).
77. Bogani, L. & Wernsdorfer, W. Molecular spintronics using single-molecule magnets. *Nat. Mater.* **7**, 179–186 (2008).
78. Woodruff, D. N., Winpenny, R. E. P. & Lay, R. A. Lanthanide single-molecule magnets. *Chem. Rev.* **113**, 5110 (2013).
79. Anshu, A., Breuckmann, N. P. & Nirkhe, C. NLTS Hamiltonians from good quantum codes. In *Proc. 55th Annual ACM Symposium on Theory of Computing* 1090–1096 (Association for Computing Machinery, 2023).
80. Rakovszky, T. & Khemani, V. The physics of (good) LDPC codes I. Gauging and dualities. Preprint at <https://arxiv.org/abs/2310.16032> (2023).
81. Motta, M. & Rice, J. E. Emerging quantum computing algorithms for quantum chemistry. *Wiley Interdiscip. Rev. Comput. Mol. Sci.* **12**, e1580 (2022).
82. Ebadi, S. et al. Quantum optimization of maximum independent set using Rydberg atom arrays. *Science* **376**, 1209–1215 (2022).
83. Bluvstein, D. et al. Logical quantum processor based on reconfigurable atom arrays. *Nature* **626**, 58–65 (2024).
84. Günther, J., Baiardi, A., Reiher, M. & Christandl, M. More quantum chemistry with fewer qubits. *Phys. Rev. Res.* **6**, 043021 (2023).
85. Vorwerk, C., Sheng, N., Govoni, M., Huang, B. & Galli, G. Quantum embedding theories to simulate condensed systems on quantum computers. *Nat. Comput. Sci.* **2**, 424–432 (2022).
86. Huggins, W. J. et al. Unbiasing fermionic quantum Monte Carlo with a quantum computer. *Nature* **603**, 416–420 (2022).
87. Scholl, P. et al. Erasure conversion in a high-fidelity Rydberg quantum simulator. *Nature* **622**, 273–278 (2023).
88. Ma, S. et al. High-fidelity gates and mid-circuit erasure conversion in an atomic qubit. *Nature* **622**, 279–284 (2023).

**Publisher's note** Springer Nature remains neutral with regard to jurisdictional claims in published maps and institutional affiliations.

**Open Access** This article is licensed under a Creative Commons Attribution-NonCommercial-NoDerivatives 4.0 International License, which permits any non-commercial use, sharing, distribution and reproduction in any medium or format, as long as you give appropriate credit to the original author(s) and the source, provide a link to the Creative Commons licence, and indicate if you modified the licensed material. You do not have permission under this licence to share adapted material derived from this article or parts of it. The images or other third party material in this article are included in the article's Creative Commons licence, unless indicated otherwise in a credit line to the material. If material is not included in the article's Creative Commons licence and your intended use is not permitted by statutory regulation or exceeds the permitted use, you will need to obtain permission directly from the copyright holder. To view a copy of this licence, visit <http://creativecommons.org/licenses/by-nc-nd/4.0/>.

© The Author(s) 2025

<sup>1</sup>Department of Physics, Harvard University, Cambridge, MA, USA. <sup>2</sup>Lawrence Berkeley National Lab, Berkeley, CA, USA. <sup>3</sup>College of Chemistry, University of California Berkeley, Berkeley, CA, USA. <sup>4</sup>Department of Chemistry, Rice University, Houston, TX, USA. <sup>5</sup>Harvard John A. Paulson School of Engineering and Applied Sciences, Harvard University, Cambridge, MA, USA. <sup>6</sup>Department of Chemistry, University of Southern California, Los Angeles, CA, USA.

✉ e-mail: [nmaskara@g.harvard.edu](mailto:nmaskara@g.harvard.edu); [lukin@physics.harvard.edu](mailto:lukin@physics.harvard.edu); [syelin@g.harvard.edu](mailto:syelin@g.harvard.edu)

## Methods

### Hamiltonian engineering

The Hamiltonian engineering toolbox introduced here is based on the average Hamiltonian approach. This approach uses the fact that, in the high-frequency limit, the effective Floquet cycle period  $K\tau$  is much smaller than the inverse local energy scales of  $H_{i,j}(p)$ , and the Floquet Hamiltonian  $H_F$  can be well approximated by expanding in a small parameter  $\frac{K\tau}{\|H(p)\|_{\text{local}}}$  (ref. 52). The leading contribution is the average Hamiltonian

$$H_F^{(0)} = \frac{1}{K} \sum_{k=0}^{K-1} H(k). \quad (8)$$

The second order term also takes a simple form

$$H_F^{(1)} = \frac{\tau}{2K} \sum_{k < k'} [H(k), H(k')]. \quad (9)$$

The results presented in the main text involve engineering the average Hamiltonian  $H_F^{(0)}$  to reproduce the target (equation (1)). In the setting where  $\theta_p$  is constant, one can apply the results of ref. 54 to construct an alternative asymptotic expansion, where each term in the Floquet Hamiltonian commutes with  $H_p$ , implying the encoding is preserved to exponentially long times  $e^{O(\|H(p)\|_{\text{local}}/K)}$ . However, in this setting, the second order term is non-zero and generates simulation errors at order  $O(\tau)$ . It can be cancelled by selecting time-reversal symmetric sequences of length  $2K$ , where the second half of the pulse is defined by  $\Theta_k = \Theta_{K-1-k}$ . This reduces simulation errors to order  $O(\tau^2)$  but might potentially alter the prethermal properties of the Floquet Hamiltonian<sup>54</sup>, which is an interesting problem for further research.

Going beyond average Hamiltonian engineering is also possible by optimizing the Floquet sequence<sup>89–91</sup>. We demonstrate engineering of higher-order terms for a small system composed of two interacting spin-3/2 particles, to controllably engineer up to bi-cubic terms ( $\hat{S}_i \cdot \hat{S}_j$ ) using only two- and three-qubit operations in Extended Data Fig. 1 and Supplementary Information section 1.

### High-spin Hamiltonian engineering with dynamical Floquet projection

Our goal is to Floquet engineer the Hamiltonian  $H = H_1 + H_p$ , in the limit  $\lambda \gg J_{ij}$ , where the system is effectively projected into the symmetric ground space of  $H_p$ . Our approach relies on implementing the combined evolution

$$U_F = \prod_{p=1}^{N_p} \left( e^{-i\theta_p \lambda^{-1} H_p} \prod_{j=1}^D e^{-itH_{i,j}} \right) \quad (10)$$

$$= \prod_{p=1}^{N_p} \prod_{j=1}^D e^{-itH_{i,j}(p)} = e^{-iK\tau H_F},$$

where  $K = N_p D$  is the full length of the sequence and  $\theta_p \lambda^{-1}$  and  $\tau$  parameterize the evolution times. To analyse this sequence, we transform into an interaction picture such that intermediate terms are evolved by  $H_p$  with a cumulative phase  $\Theta_p = \sum_{p' < p} \theta_{p'}$ ; for the rotating frame to be periodic, we require  $\Theta_{N_p+1} \pmod{2\pi} = 0$ .

Then, the transformed interactions can be written as

$$H_{i,j}(p) = e^{i\Theta_p \lambda^{-1} H_p} H_{i,j} e^{-i\Theta_p \lambda^{-1} H_p}$$

$$= \underbrace{H_{i,j}^{(0)}}_{\text{symmetric}} + \underbrace{\left( \sum_{n=1}^{n_{\max}} e^{in\Theta_p} H_{i,j}^{(n)} + \text{h.c.} \right)}_{\text{symmetry violating}}. \quad (11)$$

Here, h.c. denotes the Hermitian conjugate, and  $H_{i,j}^{(n)}$  captures unwanted terms that change the total spin on  $n$  sites, while the symmetric terms comprise the target Hamiltonian  $\sum_j H_{1,j}^{(0)} = H_T$ .

To compute the form of the interaction Hamiltonian in the rotated frame  $H_i(p) = \sum_j H_{i,j}(p)$  as used in equation (11), let us consider a single spin-1/2 particle belonging to a spin- $S_i$  cluster and define projectors  $P_i = P[\hat{S}_i^2]$  onto the symmetric space and  $Q_i = \mathbb{1} - P_i$  onto its complement. The spin-1/2 term can be split into four parts

$$\hat{S}_{i,1} = \underbrace{P_i \hat{S}_{i,1} P_i + Q_i \hat{S}_{i,1} Q_i}_{\text{symmetric}} + \underbrace{P_i \hat{S}_{i,1} Q_i + Q_i \hat{S}_{i,1} P_i}_{\text{non-symmetric}}, \quad (12)$$

where the first two terms preserve the on-site total spin and the second two change the on-site total spin. Since  $H_p$  acts as  $1 - P_i$  on the  $i$ th spin, we label terms by how they change the expectation value of  $(1 - P_i)$

$$\hat{S}_{i,1}^{(0)} = P_i \hat{S}_{i,1} P_i + Q_i \hat{S}_{i,1} Q_i \quad (13)$$

$$\hat{S}_{i,1}^{(+1)} = Q_i \hat{S}_{i,1} P_i \quad (14)$$

$$\hat{S}_{i,1}^{(-1)} = P_i \hat{S}_{i,1} Q_i. \quad (15)$$

This decomposition ensures that each term transforms under conjugation by  $H_p$ , as in equation (11), by picking up a global phase. Specifically, using the following

$$e^{-i\theta P_i} P_i = P_i e^{-i\theta P_i} = e^{-i\theta} P_i \quad (16)$$

$$e^{-i\theta Q_i} P_i = P_i e^{-i\theta Q_i} = P_i \quad (17)$$

$$e^{-i\theta P_i} Q_i = Q_i e^{-i\theta P_i} = Q_i \quad (18)$$

$$e^{-i\theta Q_i} Q_i = Q_i e^{-i\theta Q_i} = e^{-i\theta} Q_i \quad (19)$$

one can show that

$$e^{i\theta \lambda^{-1} H_p} \hat{S}_{i,1}^{(n)} e^{-i\theta \lambda^{-1} H_p} = e^{i\theta n} \hat{S}_{i,1}^{(n)}. \quad (20)$$

This rule can be extended to higher-weight operators. For example, two-spin interactions between clusters  $h_{ij} = \hat{S}_{i,1} \cdot \hat{S}_{j,1}$  decompose into five parts  $h_{ij}^{(n)}$ ,  $n = -2, -1, 0, 1, 2$ ,

$$h_{ij} = \underbrace{\hat{S}_{i,1}^{(0)} \cdot \hat{S}_{j,1}^{(0)} + \hat{S}_{i,1}^{(+1)} \cdot \hat{S}_{j,1}^{(-1)} + \hat{S}_{i,1}^{(-1)} \cdot \hat{S}_{j,1}^{(+1)}}_{h_{ij}^{(0)}} \quad (21)$$

$$+ \underbrace{\left( \hat{S}_{i,1}^{(+1)} \cdot \hat{S}_{j,1}^{(0)} + \hat{S}_{i,1}^{(0)} \cdot \hat{S}_{j,1}^{(+1)} \right)}_{h_{ij}^{(+1)}} + \text{h.c.} \quad (22)$$

$$+ \underbrace{\left( \hat{S}_{i,1}^{(+1)} \cdot \hat{S}_{j,1}^{(+1)} \right)}_{h_{ij}^{(+2)}} + \text{h.c.}, \quad (23)$$

corresponding to the different ways to change the expectation value of  $Q_i + Q_j$ . The  $n$ -spin interactions will have terms running from  $h^{(-n)}$  to  $h^{(+n)}$ . Therefore, in the rotating frame, the Hamiltonian terms transform as

$$h_{ij}^{(n)}(p) = e^{i\Theta_p \lambda^{-1} H_p} h_{ij}^{(n)} e^{-i\Theta_p \lambda^{-1} H_p} \quad (24)$$

$$= e^{i\Theta_p n} h_{ij}^{(n)} \quad (25)$$

$$h_{ij}(p) = \sum_{n=-n_{\max}}^{n_{\max}} e^{i\Theta_p n} h_{ij}^{(n)}. \quad (26)$$

We further choose a sequence of  $\theta_p$  such that only the  $h^{(0)}$  contribution is non-zero on average. The simplest sequence that satisfies these conditions is a family of cyclic pulses of order  $P$

$$\theta_p = \frac{2\pi i}{P} p \quad p = 0, \dots, P-1, \quad (27)$$

which satisfy the cancellation condition as long as  $n_{\max} < P$ . In the two-body case, of the terms that contribute to  $h_{ij}^{(0)}$ , only  $\hat{s}_{i,1}^{(0)} \cdot \hat{s}_{j,1}^{(0)}$  acts non-trivially in the symmetric subspace, so we focus on this term. An explicit form can be computed by decomposing  $\hat{s}_{i,1}$  into its permutation-symmetric and orthogonal components

$$\hat{s}_{i,1} = \underbrace{\frac{1}{2S_i} \sum_{a=1}^{2S_i} \hat{s}_{i,a}}_{\text{symmetric}} + \underbrace{\left( \frac{2S_i-1}{2S_i} \hat{s}_{i,1} - \frac{1}{2S_i} \sum_{a'=2}^{2S_i} \hat{s}_{i,a'} \right)}_{\text{non-symmetric}}. \quad (28)$$

Therefore, the symmetric part  $\hat{s}_{i,1}^{(0)} = \frac{1}{2S_i} \hat{S}_i$  is proportional to the collective spin.

With this understanding, we can construct a spin-1/2 interaction Hamiltonian  $H_i$  that recovers equation (1) under projection, by replacing each  $n$ -site high-spin interaction with an analogous spin-1/2 one. For example, for  $n=2$ , the replacement proceeds as

$$\begin{aligned} J_{ij}^{\alpha\beta} \hat{S}_i^\alpha \hat{S}_j^\beta &\rightarrow \bar{J}_{ij}^{\alpha\beta} \hat{s}_{i,a}^\alpha \hat{s}_{j,b}^\beta \\ \bar{J}_{ij}^{\alpha\beta} &= 4S_i S_j J_{ij}^{\alpha\beta}, \end{aligned} \quad (29)$$

where intra-cluster indexes  $a$  and  $b$  encode which representative from spins  $i$  and  $j$  is used to generate the interaction. The interaction strength is further boosted to  $\bar{J}_{ij}$  to account for the  $\frac{1}{2S}$  factor in equation (28). A straightforward calculation shows that, for higher-weight interactions (for example,  $n_{\max}$ ), the interaction should also be boosted (for example,  $\bar{K}_{ijk} = 8S_i S_j S_k K_{ijk}$ ) to recover the target large-spin operator under projection.

In general, it may not be feasible to uniquely assign each spin- $S_i$  interaction in  $H$  to qubits in  $H_i$  especially when a spin- $S_i$  is involved in more than  $2S$  interactions. In this case,  $H_i$  is implemented by splitting it into a sequence of non-overlapping groups  $H_{i,1}, \dots, H_{i,D}$  that approximate  $H_i$  on average. Each sequence can handle up to  $D(2S)$  interactions per spin, so if  $d$  is the interaction degree, then we require a sequence of length  $D = \lceil \frac{d}{2S} \rceil$ . Although manual decompositions sufficed for the models studied here, automated methods to determine efficient decompositions will have to be developed for more complex systems<sup>92,93</sup>.

### Multi-qubit gates with Rydberg blockade

Rydberg atom arrays are a natural platform to realize the Floquet engineering scheme described above<sup>94–98</sup>. The Rydberg Hamiltonian governing a cluster of  $N$  atoms is

$$\begin{aligned} H_{\text{cluster}} &= \frac{\Omega_q(t)}{2} \sum_i |1\rangle_i \langle 0| + \frac{\Omega_r(t)}{2} \sum_i |r\rangle_i \langle 1| + \text{h.c.} \\ &\quad + \sum_{i < j} V_{ij} |r\rangle_i \langle r| \otimes |r\rangle_j \langle r| \end{aligned}, \quad (30)$$

where  $\Omega_q(t), \Omega_r(t)$  are complex valued driving fields<sup>99,100</sup>. In the blockade approximation, which is valid when  $V_{ij} \gg \Omega_r$ , there is at most one atom in state  $|r\rangle$  (refs. 58,101). Therefore, at leading order in  $\Omega_r/V_{ij}$ ,  $H_{\text{cluster}}$  is approximated by projecting into the manifold of blockade consistent states. This produces an interacting model with an emergent permutation symmetry (see equation (S5) in Supplementary Information). This symmetry allows us to write  $H_{\text{cluster}}$  in a low-dimensional representation of the Hilbert space scaling as  $O(NN_s)$  for a representation<sup>102</sup> including the  $N_s$  largest total-spin sectors (see ‘Low-dimensional construction’ in Supplementary Information).

Figure 2b shows optimization results for an alternating ansatz with separate  $\Omega_r(t)$  and  $\Omega_q(t)$  applications (solid lines) versus a dual driving scheme with simultaneous field control (dashed lines). For the alternating ansatz, the optimization process begins with finding short sequences of symmetric diagonal gates  $D(\phi)$  and global single-qubit rotations  $Q(\theta)$  that combined realize  $U_s$  and  $U_p$  (see equation (S11) in Supplementary Information). While  $Q(\theta)$  uses global  $\Omega_q(t)$  control,  $D(\phi)$  involves multi-qubit interactions, and the pulse sequences to realize  $D(\phi)$  can be optimized through GrAPE<sup>51,59,60,103,104</sup>. Numerical optimization is feasible due to the manageable size of the low-dimensional basis. We find that the maximum gate time  $T(n)$  for generic phases (Supplementary Fig. 1). Gate times in Fig. 2 are computed by multiplying  $T(n)$  by the shortest sequence length determined in the first step. The operations  $Q(\theta)$  and  $D(\phi)$  can also be promoted to controlled operations (see ‘Alternating ansatz’ in Supplementary Information), as required for the controlled perturbation in Fig. 4a.

Dual driving gate profiles are directly optimized using GrAPE, with an added smoothness regularization to ensure driving profiles can be implemented with available classical controls (see equation (S8) in Supplementary Information and Extended Data Fig. 1). Interestingly, the optimized fidelity remains roughly independent of the system size, when tolerating noise-free error rates around  $10^{-3}$ . We select this fidelity threshold and plot the resulting gate times in Fig. 2b (dotted lines). However, for more stringent noise-free thresholds, such as  $10^{-6}$ , we observe an approximately linear dependence in  $n$ , producing gate times comparable to the alternating decomposition. Theoretical characterization of the asymptotic scaling of gate time with cluster size and error threshold remains an intriguing open question.

For comparison, we estimate gate counts for a decomposition of  $U_s$  and  $U_p$  into single- and two-qubit gates (Fig. 2c). Using the Qiskit transpiler<sup>105</sup>, we find two-qubit decompositions into single-qubit rotations and CPhase gates for  $U_p$ . For  $U_s$ , the diagonal gates  $D(\phi)$  found numerically in the alternating ansatz only require two-qubit interactions, and can be decomposed into  $\binom{n}{2}$  two-qubit CPhase gates, outperforming the Qiskit result for  $n \geq 3$ . Finally, we show in Supplementary Information that symmetric operations like  $U_s$  and  $U_p$  can be implemented with poly( $n$ ) two-qubit gates using ancilla qubits, by constructing an efficient matrix product operator (MPO) representation of arbitrary  $n$ -spin operations.

The fidelity of the multi-qubit gates is subject to errors such as spontaneous emission and dephasing due to a finite  $T_2^*$ , as seen in current Rydberg gates<sup>51</sup>. In general, errors accumulate with gate time; hence, shorter gates tend to produce higher-fidelity implementations. Certain errors can also be mitigated by improving the excitation schemes. Specifically, single-photon schemes as used in as in refs. 87,88, avoiding intermediate-state scattering, may enhance performance for bigger clusters. This is because the rate of decay from the Rydberg state does not depend on cluster size, since the number of Rydberg excitations is never larger than 1. By contrast, the rate of scattering from the intermediate state grows linearly with cluster size.

### Estimating simulation time

The simulation time is defined as the maximum evolution time, before which the typical error per qubit is below some target threshold  $\epsilon$ . We account for both coherent Hamiltonian simulation errors and incoherent gate errors. For a symmetrized sequence, we estimate the scaling of both contributions to be

$$\epsilon_{\text{sim}} = (c_2 \tau^2)^2 T^2, \epsilon_{\text{gate}} = \frac{gT}{\tau}, \quad (31)$$

with target evolution time  $T$  and step size  $\tau$ . Here, the coefficient  $c_2$  depends on the detail of the Hamiltonian simulation protocol and can be estimated from numerics or the third-order term in the Magnus

expansion (see equation (S18) in Supplementary Information). The coefficient  $g$  measures the gate error probability per cycle and is determined by assuming that each multi-qubit gate has a fixed probability of failure  $T_{\text{gate}}g_0$  that scales linearly in the time of the gate. Such a scaling is valid when errors are dominated by spontaneous emission from the Rydberg state. For simplicity, we utilize the estimated  $T_{\text{gate}}$  for large-angle unitary  $U_p$  with  $\theta = \pi$ . Both  $c_2$  and  $g$  are estimated to grow extensively in system size. Thus, we work instead with the intensive version of these quantities,  $\tilde{c}_2 = c_2/L$  and  $\tilde{g} = g/L$ .

Optimizing the step size  $\tau$  to minimize error (see ‘Heuristic simulation time estimates’ in Supplementary Information), the maximum evolution time scales as

$$T_{\text{opt}} = \frac{2^{2/3}}{5^{5/6}} \frac{\varepsilon^{5/6}/L}{(\tilde{c}_2 \tilde{g}^2)^{1/3}} \quad (32)$$

for a target error rate  $\varepsilon$ .

In Fig. 3, we use this formula, along with numerical estimates for  $c_2$  in models (i) and (ii), and heuristic estimates for models (iii) and (iv). We further estimate  $g$  using the simultaneous driving gate times of Fig. 2b and select an error per Rabi cycle of  $g_0 = 10^{-3}$ . The target error we select is  $\varepsilon^{5/6}/L = 0.1$ , which grows approximately extensively with system size. We illustrate the benefits of our approach on four example Hamiltonians (see Fig. 3 and ‘Heuristic simulation time estimates’ in Supplementary Information).

### Many-body spectroscopy

To complete our simulation framework, we also develop tools for resource-efficient readout of Hamiltonian properties. First, we illustrate how to compute two-time correlation functions of the form

$$C_{O,R}(t) = \langle S | O(t)R(0) | S \rangle, \quad (33)$$

using the circuit in Fig. 4a. The real and imaginary parts of  $C_{O,R}(t)$  are independently accessed by measuring the ancilla in the  $X$  and  $Y$  basis, respectively<sup>63,64,66,106,107</sup>. More concretely, consider the state of the system right before measurement, including both the ancilla qubit and the system

$$|\psi_t\rangle = \frac{1}{\sqrt{2}} (|0\rangle \otimes U(t)|S\rangle + |1\rangle \otimes U(t)R|S\rangle), \quad (34)$$

where  $U$  is the time-evolution operator. Measuring  $X \otimes O$  or  $Y \otimes O$  results in

$$\langle X \otimes O \rangle_{\psi_t} = \frac{1}{2} (\langle S | R^\dagger O(t) | S \rangle + \langle S | O(t)R | S \rangle), \quad (35)$$

$$\langle Y \otimes O \rangle_{\psi_t} = \frac{i}{2} (\langle S | R^\dagger O(t) | S \rangle - \langle S | O(t)R | S \rangle), \quad (36)$$

which together gives the full complex-valued  $C_{O,R}(t)$  by taking a linear combination of the two,

$$C_{O,R} = \langle (X + iY) \otimes O \rangle_{\psi_t}. \quad (37)$$

For observables  $O$  diagonal in the measurement basis,  $C_{O,R}$  can be efficiently estimated in parallel from snapshots. During the  $i$ th run, let  $\mu^{(i)} = \{x, y\}$  be the randomly sampled ancilla measurement basis and  $a^{(i)} = \{0, 1\}$ , and  $|b^{(i)}\rangle$  be the ancilla and system measurement outcomes respectively. Then, the estimator can be written as

$$\overline{C_{O,R}(t)} = \frac{1}{M} \sum_{i=1}^M 2\sigma(\mu^{(i)}, a^{(i)}) \langle b^{(i)} | O | b^{(i)} \rangle, \quad (38)$$

where  $\sigma$  is a function taking on the values

$$\begin{aligned} \sigma(x, 0) &= +1, & \sigma(x, 1) &= -1, \\ \sigma(y, 0) &= +i, & \sigma(y, 1) &= -i, \end{aligned} \quad (39)$$

and  $|b^{(i)}\rangle$  is the measured projected state.

These measurements can be used to compute the operator-resolved density of states (6), which can be rewritten as

$$\begin{aligned} D^A(\omega) &= \int dt e^{i\omega t} \sum_n \text{Tr}[A |n\rangle e^{-i\varepsilon_n t} \langle n|] \\ &= \int dt e^{i\omega t} \text{Tr}[AU(t)], \end{aligned} \quad (40)$$

where we have replaced  $\delta(\omega - \varepsilon_n) \rightarrow \int dt e^{i(\omega - \varepsilon_n)t}$ . In practice, we will sample evolution times  $t$  from a probability distribution  $p(t)$ , such that the integral is normalized to one when  $\omega = \varepsilon_n$ , that is,  $\int_{-\infty}^{\infty} p(t) dt = 1$ . To arrive at equation (7), we can replace the trace with an average over probe states<sup>108</sup>

$$\text{Tr}[AU(t)] = \mathbb{E}_{R \sim \mathcal{R}} \langle R | AU(t) | R \rangle, \quad (41)$$

where  $\mathbb{E}_{R \sim \mathcal{R}} = \text{Tr}[\mathbb{1}]^{-1} \mathbb{E}_{R \sim \mathcal{R}}$  is a normalized expectation value and  $\text{Tr}[\mathbb{1}]$  is the dimensionality of the Hilbert space. This is valid as long as the ensemble forms a two-design

$$\mathbb{E}_{R \sim \mathcal{R}} |R\rangle \langle R| = \frac{\mathbb{1}}{\text{Tr}[\mathbb{1}]}. \quad (42)$$

For example, we can sample perturbations  $R$  from the ensemble of random single-qubit rotations. Such perturbations can be implemented using the techniques from Fig. 2, by applying a sequence of two-qubit gates between an ancilla qubit and the system qubits. In general, convergence properties of the estimator depend on higher moments of  $\mathcal{R}$  (see equation (S27) in Supplementary Information).

Observables such as equation (41) can, in principle, be computed via a modified Hadamard test by applying controlled-time evolution (see ref. 64). Since time evolution is generally the most costly step, we avoid the overhead associated with controlled evolution and instead utilize a reference state  $|S\rangle$  with simple time evolution. In particular, we select an ensemble of observables  $O_s$  such that

$$\frac{1}{\mathcal{N}(O_s)} \sum_s O_s U(t) |S\rangle \langle S| U^\dagger(t) O_s = \mathbb{1}. \quad (43)$$

The normalization factor  $\mathcal{N}(O_s)$  depends on the choice of ensemble. Then, we can insert this resolution of the identity into equation (41) to get equation (7). In Figs. 4 and 5, we consider the polarized reference state  $|S\rangle = |0\rangle^{\otimes N}$ , which is an exact eigenstate of the Heisenberg Hamiltonian, and the ensemble of Pauli- $X$  operators  $O_s = X_s = \bigotimes_{i=1}^N (X_i)^{s_i}$ , where  $s$  is an  $N$ -bit string. This satisfies the condition and has  $\mathcal{N}(X_s) = 1$  since  $X_s |0\rangle^{\otimes N}$  is an orthonormal basis. For generic reference states  $|S\rangle$  prepared by applying  $S$  to  $|0\rangle^{\otimes N}$ , the ensemble  $O_s = SX_s S^\dagger$  satisfies the condition and can be measured by applying the inverse preparation circuit  $S^\dagger$  before measuring in the  $X$  basis. Lastly, an ensemble that is independent of the reference state is the set of Pauli strings  $P_s = \bigotimes_{i=1}^N \sigma_i^{s_i}$ , where  $s$  is a base-four string and  $\sigma^{s_i}$  denotes the four Pauli operators  $I, X, Y$  and  $Z$ ; this can be accessed with randomized measurements (see equations (S56)–(S57) in Supplementary Information) and has a normalization factor  $\mathcal{N}(P_s) = 2^N$ .

**Thermal expectation values.** The operator-resolved density of states can be used to compute thermal expectation values via<sup>64</sup>

$$\langle A \rangle_\beta = \frac{\int e^{-\beta\omega} D^A(\omega) d\omega}{\int e^{-\beta\omega} D^\pm(\omega) d\omega}. \quad (44)$$

For example, to compute the magnetic susceptibility, we simply select the operator  $A = \beta(S^z)^2$ , where  $\beta = 1/T$  is the inverse temperature. Interestingly, this method of estimating thermal expectation values is insensitive to uniform spectral broadening of each peak, due to a cancellation between the numerator and denominator (see discussion resulting in equation (S69) in Supplementary Information). However, it is highly sensitive to noise at low  $\omega$ , which is exponentially amplified by  $e^{-\beta\omega}$ . To address this, we estimate the SNR for each  $D^A(\omega)$  independently and zero-out all points with SNR below three times the average SNR. This potentially introduces some bias by eliminating peaks with low signal but ensures that the effects of shot noise are well controlled.

### Noise modelling

To quantify the effect of noise on the engineered time dynamics, we simulate a microscopic error model by applying a local depolarizing channel with an error probability  $p$  at each gate. This results in a decay of the obtained signals for the correlator  $D^A(t)$ . The rate of the exponential decay grows roughly linearly with the weight of the measured operators (Extended Data Fig. 2). This scaling with operator weight can be captured by instead applying a single depolarizing channel at the end of the time evolution, with a per-site error probability of  $\gamma t$  with an effective noise rate  $\gamma$ . This effective  $\gamma$  also scales roughly linear as a function of the single-qubit error rate per gate  $p$  (Extended Data Fig. 2).

### Scaling the approach

Quantum simulations are constrained by the required number of samples and the simulation time needed to reach a certain target accuracy. These factors are crucial for determining the size of Hamiltonians that can be accessed for particular quantum hardware.

Focusing on a single gapped eigenstate we determine the number of snapshots  $C_M$  needed to distinguish a spectral peak from noise (Extended Data Fig. 4). The signal arises from the overlap of the probe states with the target eigenstate. The noise is given by the variance of the estimator equation (7) and decays as  $\epsilon \approx M^{-1/2}$ . For certain ensembles of probe states, the variance can be made system size independent (see equation (S52) in Supplementary Information). However, a random probe state will have exponentially vanishing overlap with any specific eigenstate. One approach to mitigate this is to initialize probe states with higher overlap. In Extended Data Fig. 3b, we show that, for a spin-1 anti-ferromagnetic chain, a simple bond-dimension 2 MPS can outperform product states by orders of magnitude in ground-state estimation. While bond-dimension 2 states can be efficiently prepared with simple circuits of two-qubit gates, more general ansätze can also be efficiently realized using the simulation techniques described here<sup>109,110</sup>. Optimized ansätze could be further combined with importance sampling<sup>111</sup> to improve the sample efficiency of computing finite temperature or excited state properties (Supplementary Fig. 3).

The simulation time  $T_{\max}$  will depend on the required spectral resolution, which does not scale with system size for a gapped eigenstate. However, the rate of spectral broadening depends sensitively on the weight of measured observables (Extended Data Fig. 2). When the reference state is high in energy, such as the polarized state for an AFM chain, the relevant observables typically have extensive weight, requiring  $T_{\max} \approx N$  to maintain constant spectral resolution. By contrast, preparing a low-energy reference state, such as the ground state  $|S\rangle = |GS\rangle$ , allows coupling to other low-energy states using low-weight operators. This results in a noise-resilient and system-size-independent procedure (Extended Data Fig. 3). We further note that ground-state preparation can be approximate, which would result in additional spectral broadening in the computation of  $D^A(\omega)$ . While the spectral resolution requirements should also grow as the gap shrinks, we have illustrated that operator resolution can mitigate this in certain settings (for example, Figs. 5 and 6). As such, understanding the general capabilities of this approach is an interesting direction for continued research.

### OEC Hamiltonians

The OEC is a paradigmatic example of a transition-metal complex<sup>112–116</sup>. The two candidates for its closed S2 state of the OEC are parameterized with Heisenberg models  $H = -\sum_{ij} J_{ij} \hat{S}_i \cdot \hat{S}_j$  (refs. 27,117–120), and the parameters used are summarized in Supplementary Information (OEC parameters). In addition to their energies, additional information about eigenstates can be calculated by choosing the operator  $A$  in the operator-resolved density of states appropriately, and multiplying by a narrow band-pass filter in Fourier space to isolate a small set of frequencies<sup>64,121</sup>. For example, we investigate the total spin of the cubane subunit, that is, the three magnetic sites supported on opposite vertices of the cube, using  $A = (\hat{S}_1 + \hat{S}_2 + \hat{S}_3)^2$ , and compute

$$A(\omega) = \frac{D^A(\omega)}{D^1(\omega)} \quad (45)$$

evaluated at energies  $\omega_n$  of the eigenstates, which can be extracted from peaks in the spectral functions (Extended Data Fig. 5). We further use spin projection to improve the estimate in the presence of broadening. For example, if the peak at  $\omega_n$  occurs in spin sector  $P_S$ , we insert the projector  $P_S$  in the numerator and denominator,  $A(\omega_n) = \frac{D^{A P_S}(\omega_n)}{D^{P_S}(\omega_n)}$ .

### Two-dimensional Heisenberg calculations

The square lattice Heisenberg calculation was performed on a large ( $L \times L$ ) system, with Hamiltonian

$$H_{2D} = -J \sum_{\mathbf{r}} (\hat{S}_{\mathbf{r}} \cdot \hat{S}_{\mathbf{r}+x} + \hat{S}_{\mathbf{r}} \cdot \hat{S}_{\mathbf{r}+y}). \quad (46)$$

We measure the Green's function  $G(\mathbf{r}, t) = \langle S | X_{\mathbf{r}}(t) X_{\mathbf{0}} | S \rangle$  from a polarized reference  $|S\rangle^{\otimes L^2}$  (ref. 122). Since  $S^z$  is conserved under the dynamics,  $G(\mathbf{r}, t)$  is classically simulated by restricting it to the space containing the  $|S\rangle$  and single spin-flip states  $X_{\mathbf{r}} | S \rangle$ , which has dimension  $L^2 + 1$ . We evolve under equally spaced times up to  $J T_{\max} = 8$  and select  $L = 23$ , which is large enough such that  $G(\mathbf{r}, t)$  vanishes far from the boundaries. Therefore, by letting  $G(\mathbf{r}, t) = 0$  outside the simulated region, this provides a good approximation for the  $L \rightarrow \infty$  limit. As such, we define projectors onto (unnormalized) plane-wave states  $P_{\mathbf{k}} = |\mathbf{k}\rangle \langle \mathbf{k}|$ , where  $\langle \mathbf{k} | X_{\mathbf{r}} | S \rangle = e^{-i\mathbf{k} \cdot \mathbf{r}}$ . Then,  $D^{P_{\mathbf{k}}}(\omega)$  can be written as

$$D^{P_{\mathbf{k}}}(\omega) = \int dt e^{i(\omega - \omega_0)t} \sum_{\mathbf{r}} \underbrace{\langle S | X_{\mathbf{0}} P_{\mathbf{k}} X_{\mathbf{r}} | S \rangle}_{e^{i\mathbf{k} \cdot (\mathbf{r} - \mathbf{0})}} \underbrace{\langle S | X_{\mathbf{r}}(t) X_{\mathbf{0}} | S \rangle}_{G(\mathbf{r}, t)}, \quad (47)$$

which reduces to the Fourier transform  $G(\mathbf{k}, \omega)$  when the energy of the polarized state  $\omega_0$  is set to zero. Plotting this for a continuous set of  $\mathbf{k}$  and  $\omega$  produces the spectral weight depicted in Fig. 6. This further shows that finite-size systems are sufficient to simulate extended systems at finite evolution times.

By computing the peak value of  $\omega$  for each  $\mathbf{k}$  in the vicinity of the single-particle excitations, we estimate the dispersion relation  $\omega(\mathbf{k})$  associated with a single spin-flip excitation. Computations of the many-particle Green's function could be performed similarly by applying multisite perturbations, to extract finite-temperature properties and characterize the interactions between the quasi-particles.

### Data availability

All data used in this work are available via Open Science Framework at <https://doi.org/10.17605/OSF.IO/W6CTQ>.

### Code availability

All analysis codes used in this work are available via Open Science Framework at <https://doi.org/10.17605/OSF.IO/W6CTQ>.

### References

89. Kalinowski, M., Maskara, N. & Lukin, M. D. Non-Abelian Floquet spin liquids in a digital Rydberg simulator. *Phys. Rev. X* **13**, 031008 (2023).

90. Tepaske, M. S. J., Luitz, D. J. & Hahn, D. Optimal compression of constrained quantum time evolution. *Phys. Rev. B* **109**, 205134 (2023).
91. Benedetti, M., Fiorentini, M. & Lubasch, M. Hardware-efficient variational quantum algorithms for time evolution. *Phys. Rev. Res.* **3**, 033083 (2021).
92. Celi, A. et al. Emerging two-dimensional gauge theories in Rydberg configurable arrays. *Phys. Rev. X* **10**, 021057 (2020).
93. Zache, T. V., González-Cuadra, D. & Zoller, P. Fermion-qudit quantum processors for simulating lattice gauge theories with matter. *Quantum* **7**, 1140 (2023).
94. Barredo, D., De Léséleuc, S., Lienhard, V., Lahaye, T. & Browaeys, A. An atom-by-atom assembler of defect-free arbitrary two-dimensional atomic arrays. *Science* **354**, 1021–1023 (2016).
95. Cooper, A. et al. Alkaline-earth atoms in optical tweezers. *Phys. Rev. X* **8**, 041055 (2018).
96. Ma, S. et al. Universal gate operations on nuclear spin qubits in an optical tweezer array of  $^{171}\text{Yb}$  atoms. *Phys. Rev. X* **12**, 021028 (2022).
97. Singh, K., Anand, S., Pocklington, A., Kemp, J. T. & Bernien, H. Dual-element, two-dimensional atom array with continuous-mode operation. *Phys. Rev. X* **12**, 011040 (2022).
98. Jenkins, A., Lis, J. W., Senoo, A., McGrew, W. F. & Kaufman, A. M. Ytterbium nuclear-spin qubits in an optical tweezer array. *Phys. Rev. X* **12**, 021027 (2022).
99. Sheng, C. et al. High-fidelity single-qubit gates on neutral atoms in a two-dimensional magic-intensity optical dipole trap array. *Phys. Rev. Lett.* **121**, 240501 (2018).
100. Levine, H. et al. Dispersive optical systems for scalable raman driving of hyperfine qubits. *Phys. Rev. A* **105**, 032618 (2022).
101. Urban, E. et al. Observation of Rydberg blockade between two atoms. *Nat. Phys.* **5**, 110–114 (2009).
102. Arecchi, F. T., Courtens, E., Gilmore, R. & Thomas, H. Atomic coherent states in quantum optics. *Phys. Rev. A* **6**, 2211–2237 (1972).
103. Pagano, A. et al. Error budgeting for a controlled-phase gate with strontium-88 Rydberg atoms. *Phys. Rev. Res.* **4**, 033019 (2022).
104. Pedersen, L. H., Møller, N. M. & Mølmer, K. Fidelity of quantum operations. *Phys. Lett. A* **367**, 47–51 (2007).
105. Qiskit Contributors. Qiskit: an open-source framework for quantum computing. *Zenodo* <https://doi.org/10.5281/zenodo.2562111> (2023).
106. Wan, K., Berta, M. & Campbell, E. T. Randomized quantum algorithm for statistical phase estimation. *Phys. Rev. Lett.* **129**, 030503 (2022).
107. Elben, A. et al. The randomized measurement toolbox. *Nat. Rev. Phys.* **5**, 9–24 (2022).
108. Zintchenko, I. & Wiebe, N. Randomized gap and amplitude estimation. *Phys. Rev. A* **93**, 062306 (2016).
109. Haghshenas, R., Gray, J., Potter, A. C. & Chan, G. K.-L. The variational power of quantum circuit tensor networks. *Phys. Rev. X* **12**, 011047 (2022).
110. Foss-Feig, M. et al. Holographic quantum algorithms for simulating correlated spin systems. *Phys. Rev. Res.* **3**, 033002 (2021).
111. McClean, J. R., Romero, J., Babbush, R. & Aspuru-Guzik, A. The theory of variational hybrid quantum-classical algorithms. *New J. Phys.* **18**, 023023 (2016).
112. Shee, J., Loipersberger, M., Hait, D., Lee, J. & Head-Gordon, M. Revealing the nature of electron correlation in transition metal complexes with symmetry breaking and chemical intuition. *J. Chem. Phys.* **154**, 194109 (2021).
113. Pantazis, D. A. et al. Structure of the oxygen-evolving complex of photosystem II: information on the S2 state through quantum chemical calculation of its magnetic properties. *Phys. Chem. Chem. Phys.* **11**, 6788 (2009).
114. Calzado, C. J., Clemente-Juan, J. M., Coronado, E., Gaita-Arino, A. & Suaud, N. Role of the electron transfer and magnetic exchange interactions in the magnetic properties of mixed-valence polyoxovanadate complexes. *Inorg. Chem.* **47**, 5889–5901 (2008).
115. Li, X. et al. Spin Hamiltonians in magnets: theories and computations. *Molecules* **26**, 803 (2021).
116. Pokhilko, P., Bezrukov, D. S. & Krylov, A. I. Is solid copper oxalate a spin chain or a mixture of entangled spin pairs? *J. Phys. Chem. C* **125**, 7502–7510 (2021).
117. Hermele, M., Fisher, Matthew P. A. & Balents, L. Pyrochlore photons: the U(1) spin liquid in a  $S = 1/2$  three-dimensional frustrated magnet. *Phys. Rev. B* **69**, 064404 (2004).
118. Affleck, I., Kennedy, T., Lieb, E. H. & Tasaki, H. Rigorous results on valence-bond ground states in antiferromagnets. *Phys. Rev. Lett.* **59**, 799–802 (1987).
119. Kattemölle, J. & van Wezel, J. Variational quantum eigensolver for the Heisenberg antiferromagnet on the kagome lattice. *Phys. Rev. B* **106**, 214429 (2022).
120. Krewald, V. et al. Spin state as a marker for the structural evolution of nature's water-splitting catalyst. *Inorg. Chem.* **55**, 488–501 (2016).
121. Schuckert, A., Bohrdt, A., Crane, E. & Knap, M. Probing finite-temperature observables in quantum simulators with short-time dynamics. *Phys. Rev. B* **107**, L140410 (2022).
122. Knap, M. et al. Probing real-space and time resolved correlation functions with many-body Ramsey interferometry. *Phys. Rev. Lett.* **111**, 147205 (2013).

## Acknowledgements

We thank A. Aldossary, T. Betley, D. Bluvstein, M. Cain, L. Cunha, J. Feldmeier, C. Kokail, J. Lee, N. Leitao, S. Gant, J. Haber, S. Hollerith, T. Manovitz, J. Neaton, S. Sachdev, A. Schuckert, K. Seetharam and P. Zoller for insightful discussions. This work was supported by the US Department of Energy (DE-SC0021013 and DOE Quantum Systems Accelerator Center (contract no. 7568717)), the Defense Advanced Research Projects Agency (grant nos. W911NF2010021 and HRO011-23-3-0030), the National Science Foundation (via Center for Ultracold Atoms, NSF Physics Frontiers Center grant nos. PHY-2317134, Q-IDEAS HDR OAC-2118310, PHY-2207972 and PHY-2012023), the Department of Defense Multidisciplinary University Research Initiative (ARO MURI, grant no. W911NF2010082) and the Wellcome Leap Foundation under the Q for Bio programme. N.M. acknowledges support from the Department of Energy Computational Science Graduate Fellowship under award no. DE-SC0021110. A.M.G. and R.A.B. acknowledge support from the NSF through the Graduate Research Fellowships Program, and A.M.G. also acknowledges support through the Theodore H. Ashford Fellowships in the Sciences. A.I.K. acknowledges support from the US Defense Advanced Research Projects Agency (DARPA) Quantum Benchmarking Program (contract no. HRO01122C0063). J.S. and M.H.-G. acknowledge support from the NSF QCLI program through grant number QMA-2016345.

## Author contributions

N.M., S.O., M.K., M.D.L. and S.F.Y. contributed to the conception and design of Hamiltonian simulation tools. N.M., J.S. and M.H.-G. contributed to the conception and design of spectroscopy algorithms. N.M., S.O., M.K., A.M.G. and R.A.B. performed theoretical and numerical analysis. S.O., J.S. R.A.B., D.S.W., A.I.K., N.Y.Y., M.H.-G., M.D.L. and S.F.Y. contributed to the conception of the model Hamiltonian

approach. M.H.-G., M.D.L. and S.F.Y. supervised the work. All authors discussed the results and contributed to the manuscript.

### Competing interests

A.I.K. is the president and a part-owner of Q-Chem, Inc. M.H.-G. is a part-owner of Q-Chem, Inc. M.D.L. is a co-founder and shareholder of QuEra Computing, Inc. The other authors declare no competing interests.

### Additional information

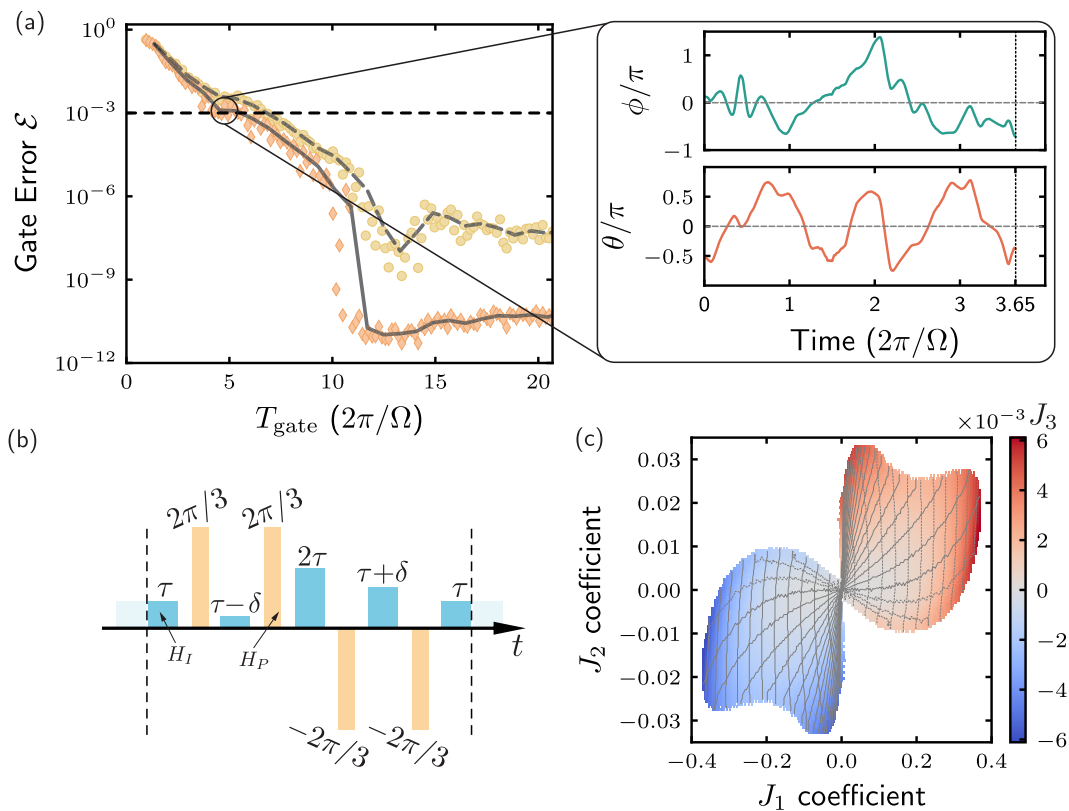
**Extended data** is available for this paper at <https://doi.org/10.1038/s41567-024-02738-z>.

**Supplementary information** The online version contains supplementary material available at <https://doi.org/10.1038/s41567-024-02738-z>.

**Correspondence and requests for materials** should be addressed to Nishad Maskara, Mikhail D. Lukin or Susanne F. Yelin.

**Peer review information** *Nature Physics* thanks the anonymous reviewers for their contribution to the peer review of this work.

**Reprints and permissions information** is available at [www.nature.com/reprints](http://www.nature.com/reprints).

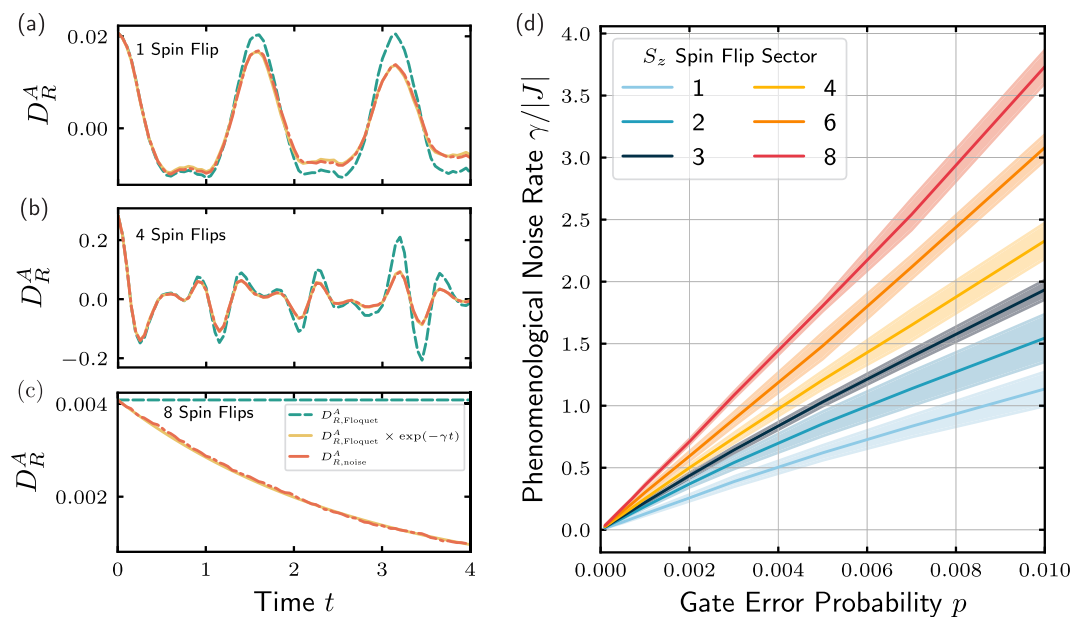


### Extended Data Fig. 1 | Gate optimization procedure and variational Hamiltonian Engineering.

(a) To find smooth gates we perform the GRAPE optimization procedure in two steps. In the first step, we penalize rapid changes in the pulse profile by introducing an extra term in the cost-function. In this case, the resulting relationship between noise-free gate-error vs. time (yellow circles) saturates around  $10^{-6}$ . For the second step we initialize the search with the smooth gates found in the previous step, which are re-optimized by removing the smooth penalty. This substantially reduces the noise-free gate error (orange). The data are shown for a  $N=4$  qubit cluster. Since the first step already confined the problem into a subspace of the search space with smooth gates, the resultant pulses also remain smooth after the second step. On the right we show an example smoothed pulse profile for the hyperfine angle  $\theta$  and the Rydberg phase  $\phi$  (see Methods) with a noise-free gate error rate  $\mathcal{E} = 10^{-3}$ . (b) Higher

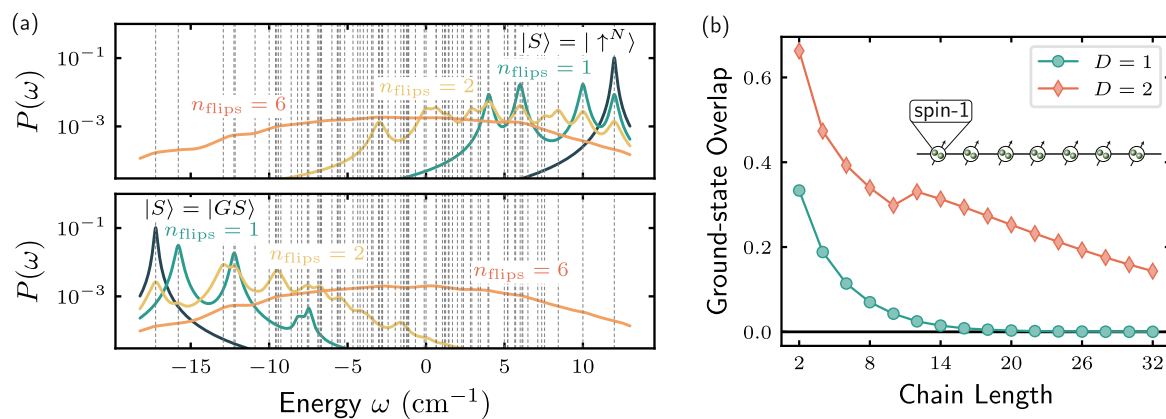
order interaction terms can be controllably engineered via a simple modification of the  $K=6$  Floquet projection sequence. For example, reducing the second time-step and increasing the fourth time-step by the same amount,  $\delta$  preserves the target Hamiltonian at leading order. (c) By tuning  $\tau$  and  $\delta$ , for a system of two interacting spin-3/2's, a very large family of coefficients  $J_1, J_2, J_3$  in the general Hamiltonian  $H_T = J_1(\hat{\mathbf{S}}_1 \cdot \hat{\mathbf{S}}_2) + J_2(\hat{\mathbf{S}}_1 \cdot \hat{\mathbf{S}}_2)^2 + J_3(\hat{\mathbf{S}}_1 \cdot \hat{\mathbf{S}}_2)^3$  can be engineered. In particular, the roughly horizontal gray lines correspond to constant  $\delta$  grid lines, and roughly vertical gray lines correspond to values with constant  $\tau$ . We see that changing  $\delta$  primarily modifies  $J_2$  and  $J_3$ , while changing  $\tau$  primarily modifies  $J_1$ , consistent with our analysis that  $\delta$  picks out certain higher-order terms. We further note that the especially interesting AKLT family, with  $J_2/J_1 = 116/243$  and  $J_3/J_1 = 16/243$  lies among the family of efficiently engineerable interactions.





**Extended Data Fig. 2 | Gate-level noise simulations.** (a)-(c) Time evolution of the correlations  $D_R^A(t)$  for a polarized reference state  $|S\rangle = |0\rangle$  and  $A$  chosen to be projectors onto different  $S_z$  sectors. This involves measuring operators of fixed weight. We see that the simulation of gate-level noise modelled as a depolarizing channel with a gate error probability  $p = 0.001$  (orange dash dotted curve) matches well with the dynamics obtained by adding an additional

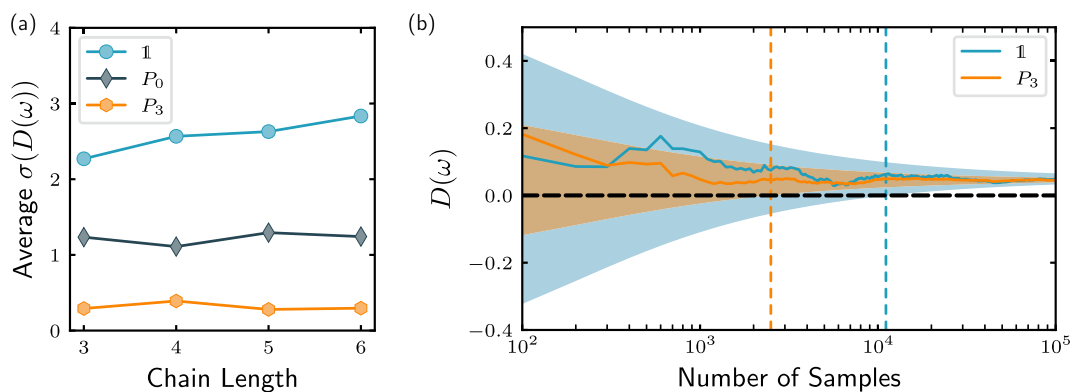
phenomenological noise  $\propto \exp(-\gamma t)$  with rate  $\gamma = (0.128, 0.251, 0.36)$  for  $N_{\text{spin flip}} = (1, 4, 8)$  (solid yellow lines) to the loss-less time evolution  $D_{R,\text{Floquet}}^A$  (green dashed). (d) Relationship between the optimal phenomenological noise rate  $\gamma$  and the gate error probability  $p$  for different spin flip sectors. We see a roughly linear-relationship of the decay rate  $\gamma$  with the gate error rate  $p$  and operator weight  $S_z$ . All data are obtained using time-steps  $\tau = 0.05$ .



**Extended Data Fig. 3 | Noise susceptibility and eigenstate overlaps. (a)**

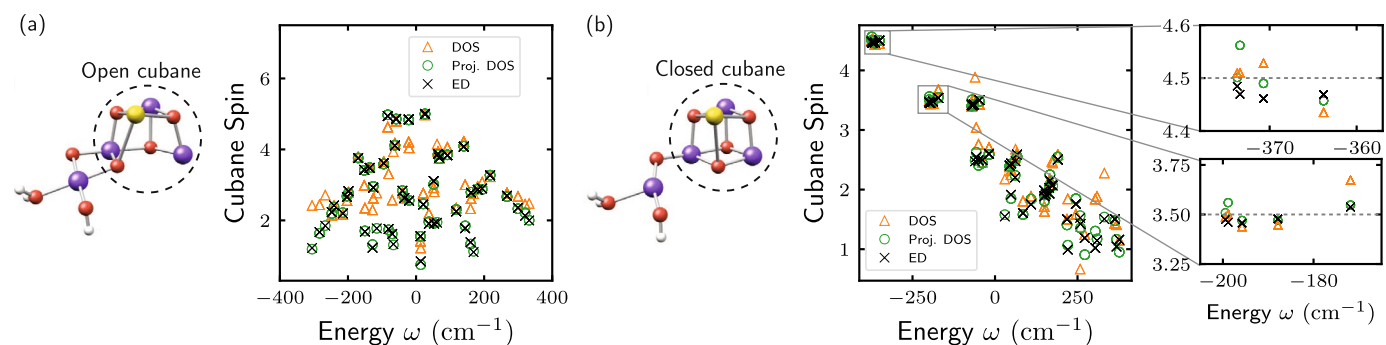
Density-of-states for a spin-1 AFM chain, computed from a polarized reference state  $|S\rangle = |0\rangle^{\otimes N}$  (top), and ground state reference  $|S\rangle = |GS\rangle$  (bottom). The spectrum is separated into sectors distinguished by their operator weight from  $|S\rangle$ . For the polarized state, these correspond to sectors with well-defined  $S^z$ . For the ground-state, each sector is orthogonalized with respect to lower-weight sectors. Each sector is phenomenologically broadened by  $e^{-\gamma n_{\text{flips}}}$  to simulate the operator-weight dependence of decoherence. When computing low-energy properties, the ground-state reference is more robust to noise, since the low-energy eigenstates can be reached with lower-weight operators. **(b)** The

amplitude of the corresponding spectral peak is determined by the eigenstate overlap. We analyze the ground-state overlap for an AFM spin-1 chain performing DMRG for low bond dimensions ( $D=1, 2$ ) and find that it is much larger for bond-dimension  $D=2$  matrix product states (red diamonds) compared to bond-dimension  $D=1$ , that is, mean-field states (green circles). Interestingly, the ground state overlap decays slower with the chain length for  $D=2$  indicating that the fidelity density is large. This feature makes low bond dimension states a promising direction for efficient state preparation within our scheme since they can efficiently be decomposed into short circuits.



**Extended Data Fig. 4 | Shot noise scaling with system size and convergence with number of snapshots.** (a) Numerically computed standard deviations of the estimator (7) for the density of states  $D^i(\omega)$  of a spin-1 AFM chain, for different chain lengths and observables. Here, we consider a polarized reference state  $|S\rangle$  and random single-qubit rotations  $R$  for the controlled-perturbation. For the bare density of states the standard deviation slowly scales with the chain length (blue circles). For the projectors into the zero (gray diamonds) and three (orange circles) spin-flip sectors the standard deviation is consistent with being

independent of system size. (b) Convergence of estimator with number of samples for two different observables. Shaded regions correspond to  $2\sigma$  error bars around the mean, and decrease with the number of measurements as  $1/\sqrt{M}$ . Dark lines are running averages for a specific sampled dataset. The sample complexity is defined as the number of samples needed such that the error bars around the mean do not include zero. After this point, spectral peaks can be reliably distinguished from noise.



**Extended Data Fig. 5 | Additional observables calculated for OEC.** By choosing  $A$  to be the local cubane spin  $\hat{S}_{123}^2$ , and calculating  $D^A(\omega)$  at each of the peaks in the density of states, we can infer the local structure of spin correlations within each eigenstate. **(a)** The cubane spin for each eigenstate for the open cubane configuration ( $S_2\text{H-1a}$ ). This model has coefficients:  $J_{12} = -15.8, J_{13} = 1.9, J_{14}, J_{23} = 23.1, J_{24} = 1.9, J_{34} = -13.9$  in  $\text{cm}^{-1}$ , and spin-sizes  $S_1 = 2, S_2 = S_3 = S_4 = 3/2$ . The triangles, circles and crosses are obtained using three different methods. The crosses indicate the exact value obtained via exact diagonalization (ED), the green circles indicate the values obtained via the spin resolved (projected) density of states

(DOS), and the orange triangles are obtained by the bare DOS. The projected DOS, which is able to resolve individual eigenstates, matches well with the ED result. In contrast the bare DOS, which has overlapping peaks (see Fig. 5), does not capture the expectation values accurately. **(b)** Same as in (a) but for the closed cubane configuration  $S_2\text{H-1b}$ . This model has  $S_1 = S_2 = S_3 = 3/2$  and  $S_4 = 2$ . We see that for the lowest-lying cluster, all spins in the cubane subunit are approximately polarized with a total spin value  $S = 9/2 = 4.5$ . In contrast, the second cluster of eigenstates seems to differ by a single spin flip as indicated by the value  $S = 7/2 = 3.5$ .